



Aeroelastic Analysis of a Morphing Wing for Airborne Wind Energy Applications

Johannes Hall

Thesis for the degree of Master of Science in
Engineering
Division of Fluid Mechanics
Department of Energy Sciences
Faculty of Engineering | Lund University



Aeroelastic Analysis of a
Morphing Wing for Airborne
Wind Energy Applications

Johannes Hall

April 2017, Lund

This degree project for the degree of Master of Science in Engineering has been conducted at the Division of Fluid Mechanics, Department of Energy Sciences, Faculty of Engineering, Lund University and at the Laboratory of Composite Materials and Adaptive Structures, ETH Zurich

Supervisor at Lund University was Dr. Robert-Zoltán Szász

Supervisor at ETH Zurich was Urban Fasel

Examiner at Lund University was Professor Dr. Johan Revstedt

The project was carried out in cooperation with Laboratory of Composite Materials and Adaptive Structures, ETH Zurich

Thesis for the Degree of Master of Science in Engineering

ISRN LUTMDN/TMHP-17/5384-SE

ISSN 0282-1990

© 2017 Johannes Hall samt Energy Sciences

Division of Fluid Mechanics

Department of Energy Sciences

Faculty of Engineering, Lund University

Box 118, 221 00 Lund

Sweden

www.energy.lth.se

Abstract

The aim of this thesis is to set up a high-fidelity fluid structure interaction (FSI) simulation environment to study the gust load alleviation capability of camber-morphing airborne wind energy (AWE) wings. The simulation environment will enable studying the transient flow phenomena around the wing when encountering wind gusts and gives the possibility of investigating dynamic instabilities.

To meet this end, an investigation on gust wind simulations is conducted. The Forcing Momentum Source method is considered the most suitable approach to simulate a discrete gust and is implemented. It allows simulating a gust of any given shape, duration and magnitude. In order to set up the fluid environment for the FSI simulation an automatic mesh generation is created using the software ICEM CFD. This generates a high quality hexahedral mesh for an arbitrary AWE wing with minimum user input. Furthermore, FSI simulations of a morphing AWE wing interacting with gust winds are carried out and different load alleviation strategies are investigated.

The AWE wing investigated in this thesis did not show any instabilities at a freestream velocity of 100 m/s. Furthermore, the wing has the ability to alleviate loads induced by a sinusoidal shaped gust wind with a magnitude of 5 m/s and a duration of 0.5 seconds.

The work of this thesis concludes that a high-fidelity FSI environment has been successfully set up. Within the environment potential load alleviation via morphing, gust interaction and dynamic instabilities can be investigated for a morphing AWE wing.

Contents

Abstract	i
List of Figures	iv
List of Tables	v
List of Symbols	vi
Abbreviations	vii
1 Introduction	1
1.1 Background	1
1.2 Motivation	6
1.3 Objectives	6
1.4 Outline of thesis	6
2 Theory	7
2.1 Gust winds	7
2.2 Wing Theory	10
2.3 Fluid governing equations and turbulence modelling	13
2.4 Structural governing equations	19
2.5 Fluid Structure Interaction	19
3 Method	23
3.1 Software	23
3.2 AWE System	23
3.3 Fluid Environment Setup	24
3.4 Structural Environment Setup	27
3.5 Fluid Structure Interaction Setup	30
3.6 Gust simulation	31
3.7 Validation	36
4 Results and discussion	40
4.1 Flow at wingtip	40
4.2 Displacement	41
4.3 Loads	45
5 Conclusion and outlook	47
5.1 Outlook	47
Bibliography	49
A Diffusion based dynamic mesh theory	52

B Implementation of gust UDFs

List of Figures

1	Conceptual comparison of conventional wind power and AWE systems	2
2	Illustration of the apparent wind speed	3
3	Illustration of the complexity of morphing wings [10]	4
4	The oscillating Tacoma Narrows Bride [12]	5
5	Example of an EOG [20]	8
6	Example of an EDC [20]	9
7	Symmetrical and cambered airfoil	10
8	Acting forces on 2D airfoil at cruise speed	10
9	Flowfield around 2D airfoil with moderate camber and AoA	11
10	Pressure forces on fluid element along a curved streamline	12
11	Illustration of tip vortices	12
12	Subdivisions of the Near-Wall region [25]	15
13	Wall function to on the left and resolved boundary layer on the right [25]	16
14	Example of a 2D control volume for the FVM [35]	18
15	Different approaches for FSI	20
16	Data transfer for the partitioned approach	21
17	Schematic illustration of aircraft for AWE system	23
18	Top left: surface mesh of wing and boundary layer mesh, top right: front view fluid domain, down: side view domain	25
19	Prisms at wing tip	26
20	Boundary conditions in the fluid environment	27
21	Structural mesh	28
22	Boundary conditions for structural environment	29
23	Thermal boundary condition for actuation	29
24	Overview of FSI	30
25	Moving inlet- and outlet boundary conditions on boundaries [44]	32
26	Velocity field of the domain with vortex based source term	33
27	Gust with sinusoidal shape, amp. of 5 m/s	35
28	Normalized lift and velocity as a function of the normalized time	36
29	C_L and C_D in convergence study	37
30	Wingtip vortex in simulation	40
31	Recirculation at wingtip	41
32	Displacement for gust interaction with no actuation	42
33	Displacement during gust interaction with no actuation	43
34	Displacement during gust interaction for case 1 actuation	43
35	Displacement during gust interaction for case 2 actuation	44
36	Displacement during gust interaction for case 3 actuation	44
37	Normalized lift for FSI simulation before gust interaction	45
38	Normalized lift during gust interaction for different actuation strategies	46

List of Tables

1	Under-relaxation factors	26
2	Boundary conditions in fluid environment, $(*) = u_i, u_j$ and u_k	26
3	Boundary conditions for grid convergence study	37
4	C_L and C_D in convergence study	37
5	Different turbulence models for medium size mesh	38
6	Domain sizes, (0,0,0) indicates point $x=y=z=0$	38
7	C_L and C_D for medium sized mesh with large and small domain	38
8	Normalized C_L and C_D for fully resolved- and wall function approach	39
9	Comparison between high-fidelity and low-fidelity results at AoA of 6 degrees	39

List of symbols

P	Power
ρ	Density
C_L	Coefficient of lift
C_D	Coefficient of drag
L	Lift force
D	Drag force
p	Static pressure
u	Flow velocity
T_{gust}	Time duration of wind gust
α	Angle of wind velocity
S	Wingspan
c	Chord
Re	Reynolds number
Φ	Arbitrary variable
$\bar{\Phi}$	Mean value of arbitrary variable
Φ'	Perturbation of arbitrary variable
μ	Dynamic viscosity
ν	Kinematic viscosity
τ	Shear stress tensor
\bar{u}	Mean velocity
u'	Velocity perturbation
\bar{p}	Mean static pressure
U^+	Dimensionless velocity
y^+	Dimensionless wall distance
ν_T	Turbulent viscosity
τ_w	Wall shear stress
u_τ	Friction velocity
κ	Von Karman constant
k	Turbulent kinetic energy
ω	Turbulent dissipation
K	Stiffness matrix
M	Mass matrix
C	Damping matrix
x_s	Structural displacement
\dot{x}_s	Structural velocity
\ddot{x}_s	Structural acceleration
\mathbf{n}	Unit vector normal to fluid structure interface
dt	time step
T	Dimensionless time
x_f	Displacement of fluid mesh at fluid structure interaction interface
u_w	Velocity of fluid at fluid structure interface
$\underline{\tau}$	Stress tensor
B	Constant in the Forcing momentum source term

Abbreviation

AWE	Airborne wind energy
CFD	Computational fluid dynamics
FSI	Fluid structure interaction
IEC	International Electrotechnical Commission
FAR	Federal Aviation Regulations
EWM	Extreme wind speed model
EOG	Extreme operating gust
ETM	Extreme turbulence model
EDC	Extreme direction change
ECD	Extreme coherent gust with direction change
EWS	Extreme wind shear
RANS	Reynold's avarage Navier Stoke's equations
URANS	Unsteady Reynold's avarage Navier Stoke's equations
LES	Large eddy simulation
DNS	Direct numerical simulation
DES	Detached eddy simulation

1 Introduction

1.1 Background

This master thesis is made in connection with the research project *Multidisciplinary Design and Optimisation of Morphing Wings for Airborne Wind Energy Applications* that is conducted in the CMAS laboratory, Swiss Federal Institute of Technology in Zürich (ETHZ). The research project is a follow up project of the *CHIRP "Smart Airfoil"* project. The *CHIRP "Smart Airfoil"* focused on the creation of adaptive structural systems. The main goal of *Multidisciplinary Design and Optimisation of Morphing Wings for Airborne Wind Energy Applications* is to apply and extend the existing optimisation tools for adaptive wings to Airborne Wind Energy (AWE) applications, and by doing so develop an adaptive structural system for AWE with an improved performance. With morphing, the wing can take the optimal shape for any flight condition [1]. This would increase the efficiency of the entire system. The research project also aims to investigate the possibility of load alleviation via morphing for AWE wings. Especially alleviate high loads due to extreme wind conditions, e.g. gust winds. This would allow to increase the safety factor of the wing without dramatically increase the mass.

The following section gives a brief introduction to AWE and morphing wings, followed by an explanation of fluid structure interaction problems. Lastly, the motivation, objectives and outline of this thesis are presented.

1.1.1 Airborne Wind Energy

In the last decades the market for renewable energy has grown radically and it is expected to continue to do so in the near future as well [2]. One of the novel technologies within renewable energy is called Airborne Wind Energy (AWE) [3]. AWE aims to convert kinetic energy in winds to electric energy, similar to conventional wind power. However, instead of a turbine being fixed on a tower, AWE systems use kites or rigid wings that are connected to the ground via a tether, see figure 1. This leads to the possibility of reaching higher altitudes, which means higher wind speeds. Higher wind speed leads to larger forces acting on the wing which in the end means a possible higher power production [4]. Another attractive feature is the possible savings in material cost in comparison to conventional wind power. This has caused numerous start ups and research groups to come up with different innovative approaches towards AWE. For example, Makani Power which is based in California uses a rigid wing whereas Kitegen in Italy uses a flexible kite [5, 6, 7].

As mentioned in the two examples above the wings of AWE systems can be either flexible or rigid. Flexible wings are mostly in the shape of kites that contain their shape due to aerodynamic loads and have the advantage of being extremely light for a given surface area. Kites are also cheaper in manufacturing in comparison to rigid wings. It is also possible to reuse a kite if it crashes. This has led to a lot of academic groups using kites. However, kites can not withstand the same force as rigid wings and typically have lower aerodynamic efficiency.

Rigid wings have the benefit of increased aerodynamic performance. A rigid wing can generally reach a higher lift to drag ratio, leading to a larger potential power output. However, manufacturing is more expensive and in the case of a wing crashing there is little chance of reusing it [3].

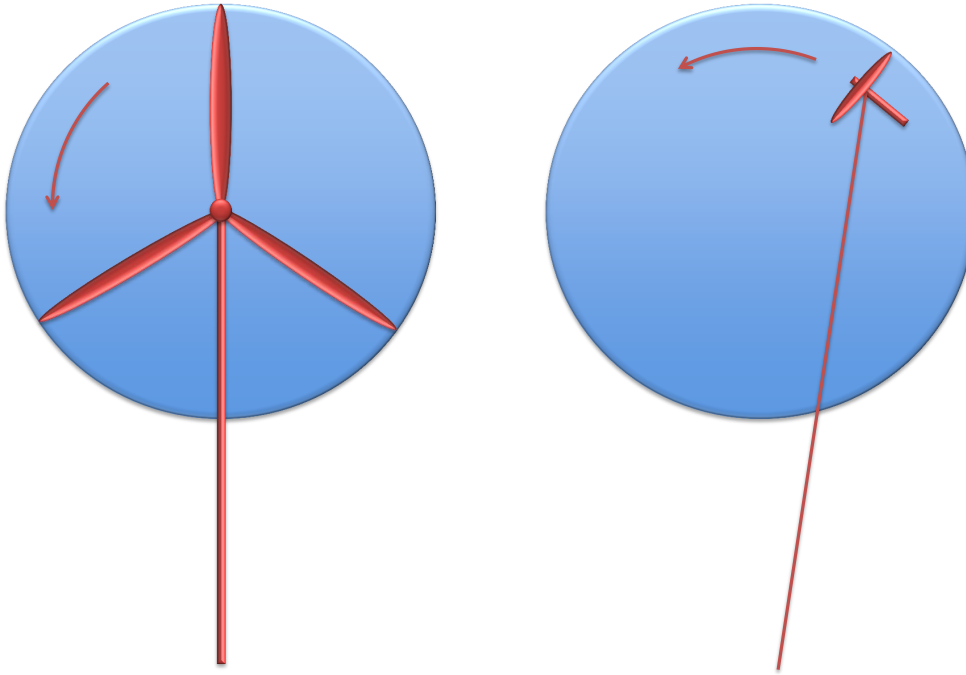


Figure 1: Conceptual comparison of conventional wind power and AWE systems

The power generation of an AWE system that uses a tethered airfoil can be divided in two groups: *lift-* and *drag mode* [8]. The drag mode uses the apparent crosswind to drive small wind turbines mounted on the tethered wing in order to generate power, whereas the lift mode uses the lift force to pull the tether to drive a generator on the ground.

The lift mode requires a flight pattern that allows for the tether to be retracted periodically. The flight pattern can be divided into two phases, the reel-in and reel-out phase. The reel-out phase is where the power generation takes place; the wing gains altitude and a large force acts on the wing and the tether. The reel-in phase actually requires some power in order to reel the wing back in. Making the reel-in phase as efficient as possible represents one of the challenges for the lift mode [3].

One large positive aspect of the drag-mode is that it does not require a reel-in phase but can generate power continuously. Furthermore, the turbines mounted on the wing can operate at high rotational speeds which makes it possible to run the system without a gearbox [3]. The turbines can also be used for vertical take off and landing. This can be done by reversing the generator and using it as a motor. However, the tether needs to be conductive to carry the electricity from the wing. The mounted wind turbines and the conducting tether typically means a heavier system and an increased drag from the tether.

Loyd introduced the following approximation for power generation, valid for both drag and lift mode [8]:

$$P = \frac{2}{27} \rho A u^3 C_L \left(\frac{C_L}{C_D} \right)^2 \quad (1.1)$$

Where A is the area of the wing, u is the wind speed and C_L and C_D the coefficient of lift and drag. Noticeable is that the lift to drag ratio influence on the power generation is to the power of two. Hence the lift to drag ratio is a very important parameter for AWE systems.

In the same paper Loyd also introduced the so called crosswind power system. By letting a wing fly in a certain pattern (circular or in the shape of an eight), perpendicular to the wind direction it is possible to increase the apparent wind speed of the wing. The apparent wind speed can be described as the wind speed from the point of view of the wing and it is this apparent wind speed that induces the total force on the wing. The relation between the direction of the wind, the flying direction of the wing and the apparent wind speed is illustrated in figure 2. Furthermore, the relationship between lift force and apparent wind speed is of a quadratic nature and is one of the keystone to why the crosswind power system is a popular strategy for AWE systems [3].

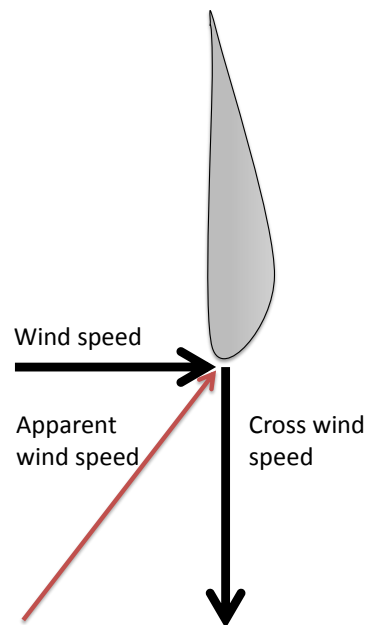


Figure 2: Illustration of the apparent wind speed

Another way to look at the benefits of the crosswind power systems is to compare it with conventional wind power. The wing of the AWE system can be representative of the tip of a blade of a wind turbine, illustrated in figure 1. For a conventional wind turbine more than half of the lift is created by the outer 30% of the blade [3]. The tether can be representative of the material cost of the tower and the inner 70% of the blade. That means for the same power output AWE would have large savings in material costs.

One of the AWE companies that is considered to be in the forefront is called Makani Power. They utilize the drag mode with several wind turbines on board the wing. Currently they have managed to create an AWE system that has a rated power output of 600 kW. The system can start to generate power at a wind speed of 4 m/s and has its full rated power at 11.5 m/s. The system uses a rigid wing, flying circular trajectories, with a radius of 145 m and operates at an

altitude of 140-310 meters.

1.1.2 Morphing wings

The term morphing means a change in shape or structure [9]. This implies that any change in shape or structure could be due to morphing. For example, one could argue that a wing with wing flaps is a morphing wing, because the shape of the wing has changed. However, the shape of the individual structure, the main wing- and wing flap by themselves, is not changing. A hawk, however, moving from low flight speed at a high altitude to a state of diving, changes the shape of its wing in order to optimise its aerodynamic performance. In this thesis, when referring to morphing, a smooth change of shape of a structure is implied rather than the change of position between two structures.

Morphing wings has been an interesting application for a long time. For example, the Wright Brothers' aircraft used wings that could be twisted as a control system [10]. The reason for the interest in morphing from an aerodynamic point of view is that depending on the flight condition the shape of the wings, or an entire aircraft, could be altered to optimise its performance. A definition of the morphing objectives can be described as "efficient, multipoint adaptability that includes macro, micro, structural and/or fluidic approaches" [11]. Once again one can refer to the hawk and how it optimises its entire appearance at different conditions. For conventional airplanes flight conditions are generally quite static during the flight. However, in take off and landing, these conditions are changed drastically.

For most applications high loads are expected to act on a wing. In order to withstand the high loads the wings are expected to be rigid and non-compliant. However, for a structure to be able to morph a certain elasticity is needed [10]. Hence, generally speaking there is a compromise that needs to be made for morphing wings: a rigid, stiff wing that can handle high loads contra an elastic wing that deforms easily. In figure 3 an illustration of the complexity with morphing wings is illustrated.

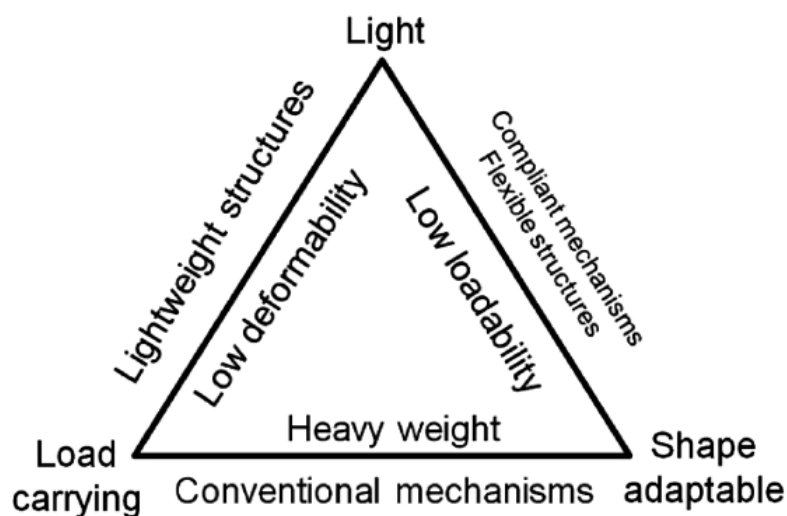


Figure 3: Illustration of the complexity of morphing wings [10]

Many different morphing wing concepts have been investigated through out the years, some more promising than others. However, the development of material technology and so called

smart systems, has opened the door to design concepts that were not possible before.

1.1.3 Fluid Structure Interaction

Essentially all fluid simulations with a solid involved are fluid structure interactions (FSI). However, many times a sole computational fluid dynamics (CFD) simulation is good enough of an approximation. This is when the deformations of the structures due to the pressure induced by the fluid are so small that they can be neglected. One could also transfer the loads from a CFD solution to a structure to see how it reacts. This is called a 1-way FSI simulation.

For other cases deformations of the structure are large enough to affect the flow and are important to take into consideration. Sometimes the forces that act on the structure can cause oscillatory behaviour which can lead to structural failure. Or the flow may simply induce a pressure large enough to deform the structure to the point where it breaks. For these cases a 2-way FSI simulation is more appropriate, considering the solution of the structural and fluid part will affect each other.

A classic example of FSI in reality is the collapse of the Tacoma Narrows Bridge in 1940. The bridge collapsed due to aerodynamic forces caused by high wind speeds. This caused the bridge to oscillate and finally collapse [12]. In figure 4 the oscillating bridge is shown.

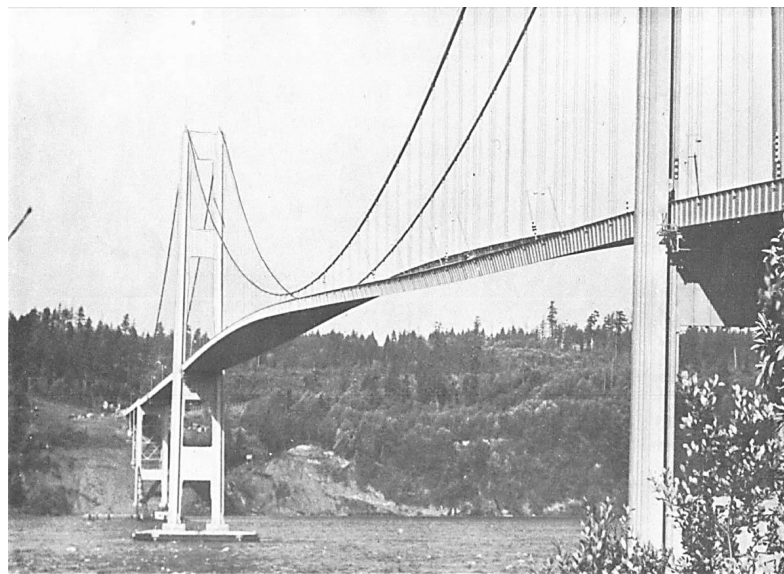


Figure 4: The oscillating Tacoma Narrows Bridge [12]

Today it is common to try and simulate FSI problems in order to understand the physics of a certain application. Typical industries include aerospace- and pharmaceutical companies. In the case of the aerospace industry a typical application is to investigate wing flutter [13]. For pharmaceutical applications it is common to investigate the blood flow, for example through an artery. Because of the elastic behaviour of the artery the fluid will deform its walls [14].

FSI solvers exist both in open source code and in commercial software and depending on the problem one would like to solve, different approaches towards the FSI modelling can be taken. The theory behind the different approaches will be further discussed in section 4.4.

1.2 Motivation

Morphing wings tend to be more elastic than rigid wings. At the same time, wings optimised for airborne wind energy are expected to work with high loads acting on them. This combination makes for large deformation of the wing due to the forces induced by the flow. Hence, a 2-way fluid structure interaction (FSI) is the most appropriate approach to simulate the case.

The current tools being used in the research project to optimise the adaptive structure for the AWE system are based on low fidelity aerodynamic simulations that are weakly coupled to a structural solver that uses the finite element method [15]. Here the nonlinear extended lifting line method [16] is used to calculate the 2D sectionwise aerodynamic characteristics via the software XFOIL [17]. This makes it a fast method that gives sufficient accuracy for preliminary wing design. However, turbulent-, unsteady- and large 3D effects (e.g. induced drag due to tip vortices) are not fully resolved. In AWE applications high loads are expected to act on the wings, meaning the wings are likely to be cambered and flying at a high angle of attack. This makes it important to validate the results of the low-fidelity optimisation with a high-fidelity simulation that can take into account the turbulent-, unsteady- and large 3D effects.

Furthermore the low fidelity tools cannot capture the transient behaviour of the wing. This is important in order to investigate the interaction of the wing with gust winds and how to actuate the wing in order to alleviate extreme loads. This means a method to analyse how the wing behaves when it interacts with gust winds and the possibility to actively morph the wing in a manner that would alleviate loads is needed.

1.3 Objectives

The objectives of this thesis are presented below.

- Set up a high fidelity fluid-structure interaction (FSI) simulation environment for AWE morphing wings.
- Analyse different strategies for gust simulation and implement the most promising one in the high fidelity environment.
- Use the FSI high-fidelity environment to analyse the dynamic behaviour of the AWE morphing wing at extreme load conditions (gust winds) as well as actuation strategies and compare with low-fidelity results.
- Identify areas of improvement for the wing design in order to maximise the power extraction for AWE application and morphing requirements for the shape-adaptive wings.

1.4 Outline of thesis

After the introduction the theory used in this thesis is presented. This is followed by the method used to conduct the simulations. After the method the results of the are shown and discussed and the last chapter presents a conclusion followed by an outlook for the thesis.

2 Theory

In this section the theory and important definitions are introduced. First is an explanation of gust winds and existing standards. This is followed by general conventions and theory for wings. When this is done the governing equations for the simulations in this thesis are presented. The derivations for the governing equations can be found in many textbooks covering computational fluid dynamics or computational structural dynamics and will not be included in this thesis.

2.1 Gust winds

Gust winds can be described as differences in the wind speed in a turbulent velocity field. This is a broad description which leaves room for many different shapes, lengths and magnitudes of gust winds, which is also true in reality. However, gust winds typically represent extreme conditions for aircraft and wind turbines [18, 19]. Due to this, different standards exist in order to categorise gust winds. Two standards that are used is the International Electrotechnical Commission (IEC) 61400-1 [20] and the Federal Aviation Regulations (FARs) [21]. Where FARs includes standards for aircraft the IEC 61400-1 standard gives a variety of working conditions for wind turbines, including gust winds and extreme loading conditions. This thesis focuses on the IEC 61400-1 standard due to the similarities between AWE systems and conventional wind power systems.

In IEC 61400-1 samples of wind speed are averaged over 10 minutes. These samples are referred to as the mean average wind speed. Hence the standard considers the time scale of gust winds less than 10 min. Gusts are treated as statistical recurring events. For example one can design a wind turbine for the worst case scenario gust that would happen every 50 years. This is derived from statistical data.

The standard introduces six extreme wind conditions:

- *Extreme wind speed model (EWM):*
- *Extreme operating gust (EOG):*
- *Extreme turbulence model (ETM):*
- *Extreme direction change (EDC):*
- *Extreme coherent gust with direction change (ECD):*
- *Extreme wind shear (EWS):*

Following is an introduction to EOG, EDC and ECD. These are the standardized extreme wind conditions taken into consideration in this thesis.

2.1.1 EOG

For the EOG situation the gust would typically have the appearance of a so called "1-cosine"-gust. Here there is no change in the direction of the wind, only a change in speed. It is modelled with the following equation:

$$u(z, t) = U - 0.37U_{gust} \sin(3\pi t/T_{gust})(1 - \cos(2\pi t/T_{gust})) \quad (2.1)$$

Where $u(z, t)$ is the time dependent velocity, U is the mean free stream velocity and U_{gust} is the maximum amplitude of the gust, t represents the time and T_{gust} the duration of the gust wind. An example of an EOG is shown in figure 5.

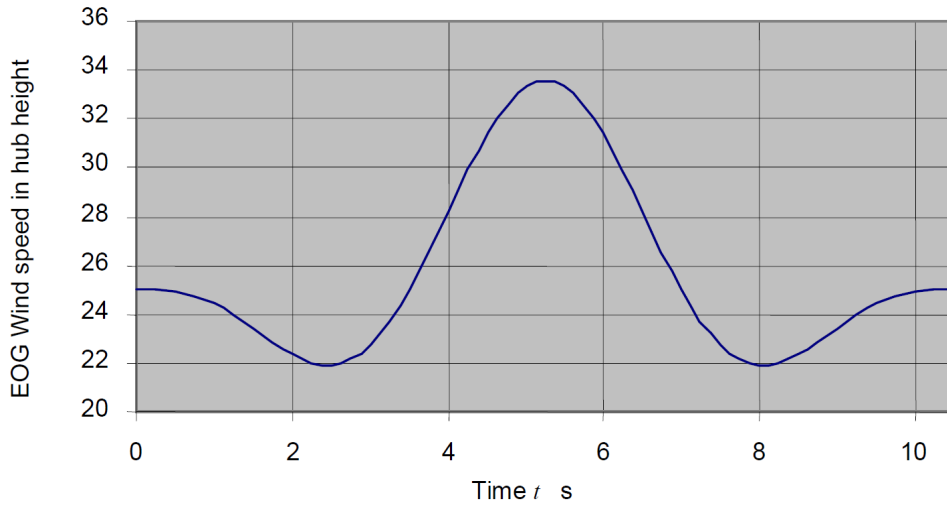


Figure 5: Example of an EOG [20]

2.1.2 EDC

The EDC does not model an increase in wind speed but rather a change in the direction of the velocity. For a wing this leads to a change in angle of attack which would increase respectively decrease the lift force acting on the wing. In the case of an AoA that is already considerably high, and further increased by the EDC, there is a risk of unsteady turbulent phenomena such as separation.

Here the transient direction change is modelled as:

$$\theta(t) = \pm 0.5\theta_e(1 - \cos(\pi/T_{gust})) \quad (2.2)$$

where θ_e is the final direction change of the wind velocity, further defined in the standard. in figure 6 an example of a EDC is shown.

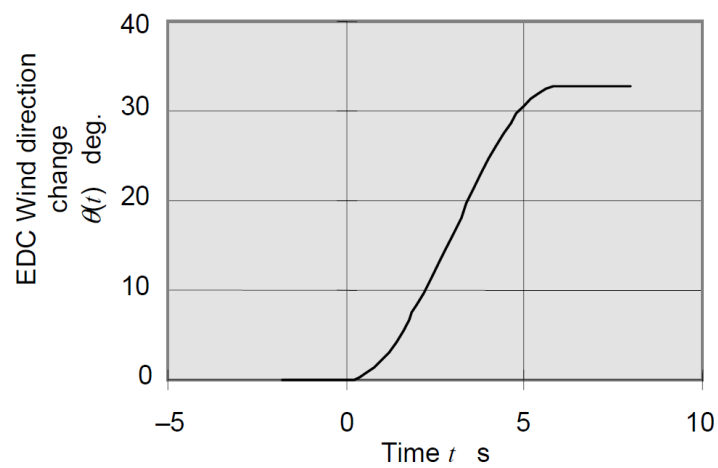


Figure 6: Example of an EDC [20]

2.1.3 ECD

In the case of an ECD event there is a change in the mean stream velocity as well as a change in the direction of the velocity. A change in the mean stream velocity does not necessarily implies an extreme wind event but if the rise takes place during a short time and with a change in velocity it might cause a dangerous scenario for the AWE system.

2.2 Wing Theory

2.2.1 Conventions

When speaking of an airfoil there is some terminology that is important to know about that will be used in this thesis. This is presented in figure 7.

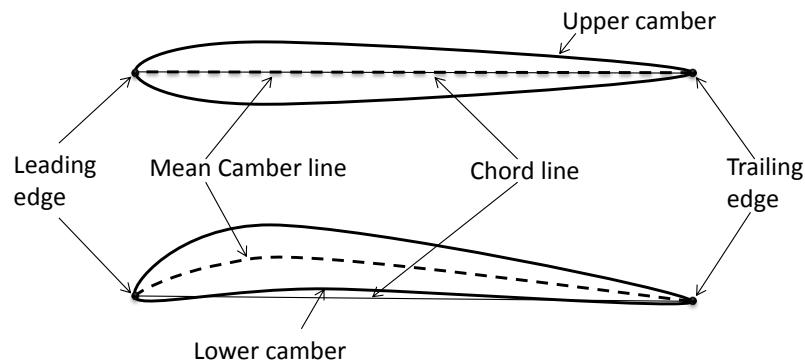


Figure 7: Symetrical and cambered airfoil

The leading edge is the foremost part of the airfoil that separates the flow, the trailing edge is the rear edge where the flow is rejoined again. The Chord line is the shortest distance between the leading- and trailing edge and the mean camber line is defined as the curvature of the median line between the upper and lower camber.

As can be seen for non cambered (symmetrical) airfoil the chord line and the mean chord line are each others tangents.

2.2.2 Forces

The forces that acts on an wing in 2 dimensions are called Drag and Lift [22]. Lift representing a force perpendicular to the airflow and drag in the same direction as the airflow. For example, when an airplane is cruising the lift force is in equilibrium with the gravitational force and the drag force in equilibrium with the thrust force from the propulsion system, see figure 8.

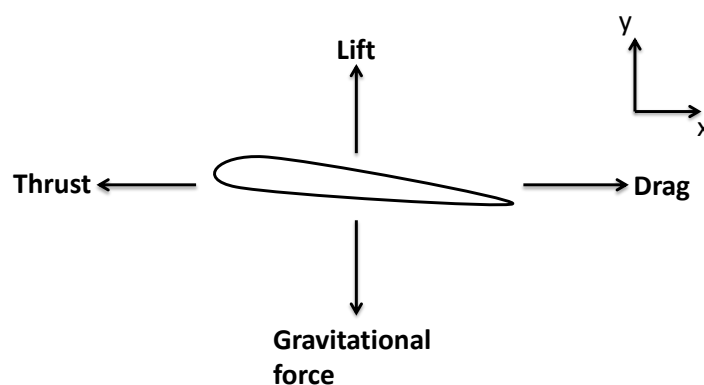


Figure 8: Acting forces on 2D airfoil at cruise speed

The origin of the lift force is a widely discussed subject that has led to many heated debates in the past and is still discussed today. Several explanations exists, some relying on math others

on physical phenomena, some are more accurate than others and some are just plain wrong [23]. With this in mind, no attempt to explain the hole origin of the lift force will be done. However, the importance of the camber will be discussed due to its importance in the morphing application simulated in this thesis. In order to explain this in a physical way, the flow field around an airfoil of moderate camber and angle of attack is accepted, not explained, to appear as in figure 9. What is accepted in this picture is that the streamlines are curved, resulting in a down wash of the air when leaving the airfoil.

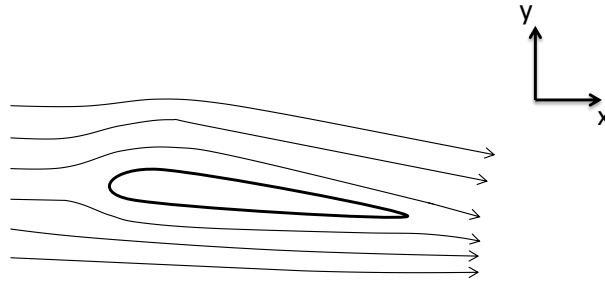


Figure 9: Flowfield around 2D airfoil with moderate camber and AoA

When this flow field is accepted one can look closer on a curved surface with a flow going over it, see figure 10. Here a fluid element is examined and the streamline that this fluid element follows is illustrated with an arrow. The pressure acting on the side of the fluid element closer to the surface must be lower than the pressure acting on the fluid element side further away if an acceleration normal to the streamline is to take place. Without this pressure difference, the streamline would not be curved. This means that a flow over a convex surface results in a pressure on this surface, lower than the ambient pressure. In the case of a cambered wing, this would mean a pressure difference between the lower and the upper surface which results in a force in the positive y -direction. This also means, if the curvature is steeper a greater pressure difference is expected, leading to a larger force and the other way around. Hence, by cambering an airfoil the lift force acting on the airfoil is expected to increase, and the other way around.

This is one way of explaining the importance of camber when it comes to the lift force acting on an airfoil. Alternative explanations exist as well but these will not be further investigated in this thesis.

The lift force is calculated by integrating the pressure on the upper and lower surface as well as adding shear forces acting perpendicular to the mean flow.

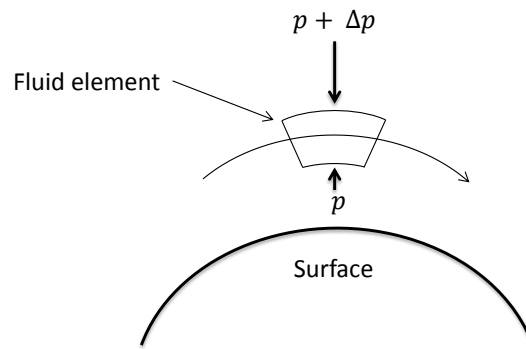


Figure 10: Pressure forces on fluid element along a curved streamline

The drag of a wing can be divided into three main groups: the induced drag, the skin friction drag and the pressure drag [22]. The pressure drag has its origin in the pressure difference occurring upstream and downstream of the wing and the skin friction is the drag induced due to the shear stress on the interface between the air and the wing. The pressure drag and skin friction drag together is usually called the profile drag. The induced drag is a little more complex and is actually only present in the case of a finite wing in three dimensions. It occurs due to the pressure difference between the lower and upper surface of the wing. At the tip of the wing the air on the lower part will tend to flow around the tip towards the lower pressure on the upper surface of the wing. The air flowing from the lower surface to the upper interferes with flow that goes over the wing in chordwise direction. The interference leads to so called tip vortices that causes a downwash of the air downstream of the tip. The creation of these tip vortices changes the flow over the wing, causing the lift force acting on the wing for a finite wing with a certain angle of attack in 2D to be smaller for a finite wing with the same conditions in 3D. This means that in order to have the same lift force acting on the wing, the angle of attack must be increased, which in turn increases the drag. It can be shown that the induced drag is at its minimum for an elliptic lift distribution over the wingspan. This can be achieved with an elliptic shape of the wing. In figure 11 the wing tip vortices for a 3D finite wing are illustrated.

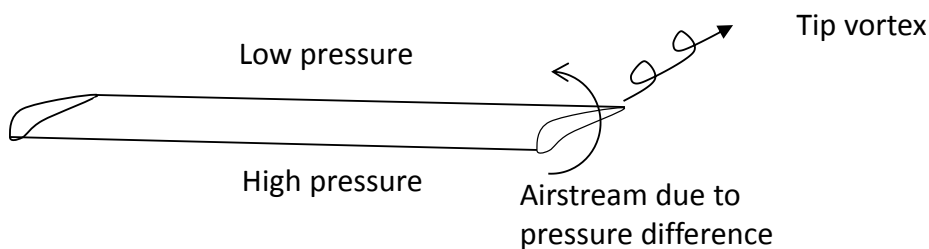


Figure 11: Illustration of tip vortices

2.2.3 Dimensionless coefficients and numbers

When discussing the behaviour of a wing one usually refers to normalised coefficients [22]. In this thesis the two normalized coefficients taken into account are the coefficient of lift, C_L , and the coefficient of drag C_D .

$$C_L = \frac{2L}{\rho u_{free}^2 A} \quad (2.3)$$

$$C_D = \frac{2D}{\rho u_{free}^2 A} \quad (2.4)$$

Where L is the lift force and D is the drag force. u_{free} is the freestream velocity and A is a characteristic area. For example, in the case of a rectangular wing $A = S \cdot c$, where S is the wingspan and c the chord length [22]. Another important definition that is commonly used whenever any flow is discussed is the Reynolds number.

$$Re = \frac{\rho u L}{\mu} \quad (2.5)$$

Where ρ is the density, u the velocity, L a characteristic length and μ the dynamic viscosity. The Reynolds number describes a relation between inertial- and viscous forces. Another way to look at it is the ratio of the total momentum transfer to the molecular momentum transfer. What the Reynolds number then can indicate, is whether or not viscosity or convection is dominant in terms of momentum transfer. If viscosity is dominant, it will dissipate any chaotic motions - leaving the flow laminar. If convection is dominant however, chaotic motions will be free to roam, typical for a turbulent flow [24]. Turbulence will be further discussed in section 2.2.2.

2.3 Fluid governing equations and turbulence modelling

2.3.1 Navier Stoke's equations

The equations that are solved for the fluid part of the simulation are the so called Navier Stoke's equations. With an assumption of an isentropic flow, the energy equation can be neglected, hence only the continuity- and the momentum equation are presented [25].

$$\frac{\partial \rho}{\partial t} + \frac{\partial(\rho u_i)}{\partial x_i} = 0 \quad (2.6)$$

$$\rho \left(\frac{\partial u_i}{\partial t} + u_j \frac{\partial u_i}{\partial x_j} \right) = \rho g_i - \frac{\partial p}{\partial x_i} + \frac{\partial \tau_{ij}}{\partial x_j} \quad (2.7)$$

For an incompressible, Newtonian fluid the momentum equation can be simplified.

$$\rho \left(\frac{\partial u_i}{\partial t} + u_j \frac{\partial u_i}{\partial x_j} \right) = -\frac{1}{\rho} \frac{\partial p}{\partial x_i} + \nu \frac{\partial^2 u_i}{\partial x_j^2} \quad (2.8)$$

And if the flow is considered steady the continuity- and momentum equations are reduced.

$$\frac{\partial u_i}{\partial x_i} = 0 \quad (2.9)$$

$$u_j \frac{\partial u_i}{\partial x_j} = -\frac{1}{\rho} \frac{\partial p}{\partial x_i} + \nu \frac{\partial^2 u_i}{\partial x_j^2} \quad (2.10)$$

2.3.2 Turbulence

"Big whirls have little whirls which feed on their velocity. Little whirls have lesser whirls and so on to viscosity – in the molecular sense"

This is how L. F. Richardson described turbulence in his book *Weather Prediction by Numerical Process* [26]. Turbulence lacks a definition but can be described with certain characteristics, *random motion* perhaps being the most intuitive.

Even though there is a lack of definition of turbulence, that has not stopped people from trying to model it. Generally speaking there are three different main approaches to model turbulence today: RANS equations, Large eddy simulation (LES) and Direct numerical simulation (DNS). Hybrid forms of these have also been made, such as detached eddy simulation (DES) [27]. In the scope of this thesis only the RANS equations will be discussed. The reason for this is that none of the other methods will be used and are left for the reader to discover by their own interest.

2.3.3 RANS equations

When trying to model turbulence a common way to do this is with the Unsteady or Steady Reynold's Averaged Navier Stoke's equations (RANS or URANS) [27]. They can be derived from equation 2.6 and 2.7 by applying Reynold's decomposition where a quantity is decomposed into a time averaged part represented by $\bar{\Phi}$ and a fluctuating part represented Φ' .

$$\Phi = \bar{\Phi} + \Phi' \quad (2.11)$$

Which after some further derivation leads to the URANS-equations.

$$\frac{\partial \bar{u}_i}{\partial x_i} = 0 \quad (2.12)$$

$$\frac{\partial \bar{u}_i}{\partial t} + \bar{u}_j \frac{\partial \bar{u}_i}{\partial x_j} = -\frac{1}{\rho} \frac{\partial \bar{p}}{\partial x_i} + \nu \frac{\partial^2 \bar{u}_i}{\partial x_j^2} - \frac{\partial}{\partial x_j} (\overline{u'_i u'_j}) \quad (2.13)$$

for a steady state condition the time-dependent term $\frac{\partial \bar{u}_i}{\partial t}$ can be assumed to be negligible which gives the RANS-equations,

$$\bar{u}_j \frac{\partial \bar{u}_i}{\partial x_j} = -\frac{1}{\rho} \frac{\partial \bar{p}}{\partial x_i} + \nu \frac{\partial^2 \bar{u}_i}{\partial x_j^2} - \frac{\partial}{\partial x_j} (\overline{u'_i u'_j}) \quad (2.14)$$

The observant reader notices that the last term in 2.13 and 2.14, $\overline{u'_i u'_j}$, introduces new unknowns to the equations. This term is called the Reynold's stress tensor and this is the term that is modelled when applying the RANS-equations in order to close the system of equations. Different models exist that model the term, so called turbulence models. One famous assumption that many of these turbulence models are based on is the Boussinesq eddy viscosity assumption [28]. This assumption introduces a quantity called *turbulent viscosity* or *eddy viscosity*. The turbulent viscosity would act in a way similar to molecular viscosity which describes momentum

transferred due to molecular motion. However, the turbulent viscosity describes momentum transfer caused by turbulent motion.

Based on the fact that the URANS-equations are time averaged one might question using them for transient flows and in some cases the validity of the URANS-equations are rightfully questioned. The URANS-equations describe a mean flow. The mean flow is simulated over a certain time, divided into a number of time steps. By assuming that the time scale of the mean flow, i.e. the time step, is much larger than the largest time scale of the turbulent motion, the turbulent motion can be described as a mean flow characteristics within each time step. Hence no turbulent motion is fully resolved but modelled as part of the overall mean flow.

If the time scale of the mean flow and the time scale of the turbulent motion is in the same order, the turbulent motion would be resolved and the solution would not longer be a mean flow. This also applies for space. A mesh that is very fine might start resolve turbulent motions that are not a mean characteristic. While this is the goal for LES and DNS simulations, the URANS-equations are meant to solve mean flows rather than resolving turbulent motion.

2.3.4 Wall Flows

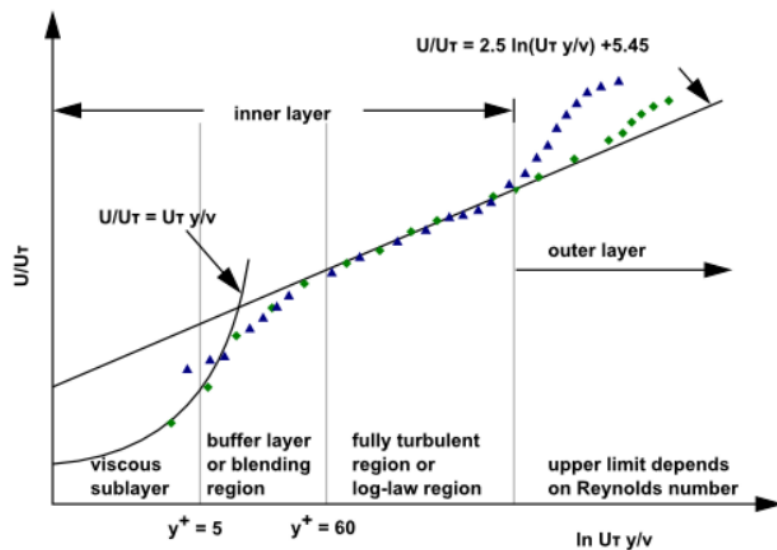


Figure 12: Subdivisions of the Near-Wall region [25]

Close to the wall of the structure the flow behaves in a certain way. Here, a boundary layer is created due to the friction in the interface between the fluid and the wall. If the flow moves dominantly in the direction tangential to the wall, as in the case for a flat plate or an airfoil, the velocity for all directions is assumed to be zero for the fluid, at the wall. Moving further away from the wall there will be an increase in the tangential velocity of the flow until the free stream velocity is reached [27]. The shape of the velocity profile in the boundary layer is dependent on if the flow is laminar or turbulent. Only the turbulent case will be discussed in this thesis.

When discussing the flow close to the wall one usually refers to the dimensionless velocity and the dimensionless wall distance,

$$U^+ \equiv \sqrt{\frac{\tau_w}{\rho}} \quad (2.15)$$

$$y^+ \equiv \frac{\rho u_\tau y}{\mu} \quad (2.16)$$

where τ_w is the wall friction. By plotting U^+ as a function of y^+ the shape of the boundary layer can be shown. An example of this is showed in figure 12. This is a general case for wall-bounded flows and the relation between U^+ and y^+ is called the Law of the Wall. The Law of the Wall is an empirical relation that has been shown through experiments, e.g. [29]. It can be described with the following equations:

$$U^+ = \frac{1}{\kappa} \ln(Ey^+) \quad (2.17)$$

where,

κ = Von Karman constan (= 0.4187)

E = emperical constant (= 0.9793)

With this in mind there are two possible ways to model the boundary layer in a simulation. In order to fully resolve the boundary layer a $y^+ \approx 1$ is needed, or one can utilise the Law of the Wall and have the first node at $y^+ \approx 30$. However, in case of separation the Law of the Wall is not valid. Figure 13 shows an illustration of the two different cases.

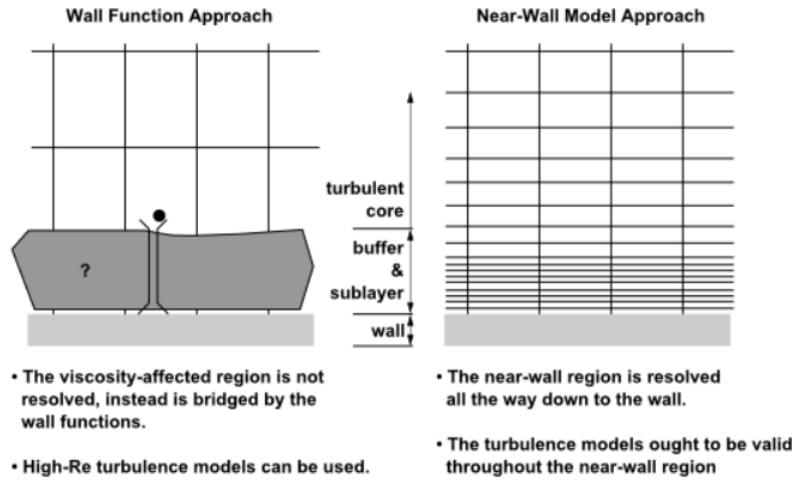


Figure 13: Wall function to on the left and resolved boundary layer on the right [25]

2.3.5 $k - \omega$ -SST turbulence model

The $k - \omega - SST$ -model is widely used for aerodynamic applications [30]. It can be described as a combination of the $k - \epsilon$ -model and the $k - \omega$ -model; the region close to the wall is modelled with the $k - \omega$ -model whereas the free stream is modelled with the $k - \epsilon$ -model [31, 32].

The following equations are used for the $k - \omega - SST$ -model [33],

$$\nu_T = \frac{a_1 k}{\max(a_1 \omega, SF_2)} \quad (2.18)$$

$$\frac{\partial k}{\partial t} + U_j \frac{\partial k}{\partial x_j} = P_k - \beta^* k \omega + \frac{\partial}{\partial x_j} \left[(\nu + \sigma_k \nu_T) \frac{\partial k}{\partial x_j} \right] \quad (2.19)$$

$$\frac{\partial \omega}{\partial t} + U_j \frac{\partial \omega}{\partial x_j} = \alpha S^2 - \beta \omega^2 + \frac{\partial}{\partial x_j} \left[(\nu + \sigma_\omega \nu_T) \frac{\partial \omega}{\partial x_j} \right] + 2(1 - F_1) \sigma_{\omega 2} \frac{1}{\omega} \frac{\partial k}{\partial x_i} \frac{\partial \omega}{\partial x_i} \quad (2.20)$$

Here ν_T represents the turbulent viscosity, k the turbulent kinetic energy and ω the turbulent dissipation. F_2, P_k and F_1 are auxiliary relations and $\alpha_1, \beta_1, \beta_2, \beta^*, \sigma_{k1}, \sigma_{k2}, \sigma_{\omega 1}$ and $\sigma_{\omega 2}$ are constants.

2.3.6 Spalart-Allmaras turbulence model

The Spalart-Allmaras turbulence model is widely used for aerodynamic applications in industry and research. It solves a transport equation for a viscosity-like variable, $\tilde{\nu}$. Due to this the model only needs to solve one equation which potentially reduces computational time [34].

$$\nu_t = \tilde{\nu} f_{v1}, \quad f_{v1} = \frac{\chi^3}{\chi^3 + C_{v1}^3}, \quad \chi := \frac{\tilde{\nu}}{\nu} \quad (2.21)$$

$$\frac{\partial \tilde{\nu}}{\partial t} + u_j \frac{\partial \tilde{\nu}}{\partial x_j} = C_{b1} [1 - f_{t2}] \tilde{S} \tilde{\nu} + \frac{1}{\sigma} \{ \nabla \cdot [(\nu + \tilde{\nu}) \nabla \tilde{\nu}] + C_{b2} |\nabla \tilde{\nu}|^2 \} \quad (2.22)$$

$$- [C_{w1} f_w - \frac{C_{b1}}{\kappa^2} f_{t2}] \left(\frac{\tilde{\nu}}{d} \right)^2 + f_{t1} \Delta U^2 \quad (2.23)$$

$$\tilde{S} \equiv S + \frac{\tilde{\nu}}{\kappa^2 d^2} f_{v2}, \quad f_{v2} = 1 - \frac{\chi}{1 + \chi_{v1}} \quad (2.24)$$

$$f_w = g \left[\frac{1 + C_{w3}^6}{g^6 + C_{w3}^6} \right]^{1/6}, \quad g = r + C_{w2} (r^6 - r), \quad r \equiv \frac{\tilde{\nu}}{\tilde{S} \kappa^2 d^2} \quad (2.25)$$

$$f_{t1} = C_{t1} g_t \exp(-C_{t2} \frac{\omega_t^2}{\Delta U^2} [d^2 + g_t^2 d_t^2]) \quad (2.26)$$

$$f_{t2} = C_{t3} \exp(-C_{t4} \chi^2) \quad (2.27)$$

Here S is the magnitude of the vorticity, d is the distance to the closest wall, $\sigma, C_{b1}, C_{b1}, \kappa, C_{w1} = C_{b1}/\kappa^2 + (1 + C_{b2})/\sigma, C_{w2}, C_{w3}, C_{v1}, C_{t1}, C_{t2}, C_{t3}$ and C_{t4} are constants.

2.3.7 Transition $k - \omega$ SST turbulence models

The transition $k - \omega$ SST turbulence couples two other transport equations with the original $k - \omega$ -SST turbulence model. One of the additional transport equations is for the intermittency and the other one is for the transition onset criteria. This is done in order to improve the accuracy of the transition from laminar to turbulent boundary layer [25].

2.3.8 Finite Volume Method (FVM)

The partial differential equations that the governing equations of the fluid simulations consists of can not be solved analytically. They are therefore solved using numerical methods. In order to do this the equations must be discretised. This is done by converting the partial differential equations to algebraic equations. Furthermore a computational domain is created by dividing the region of interest into small cells that are built up by nodes which contains computational quantities.

Here, the FVM is used to discretize the fluid computational domain. It creates its computational space by dividing the computational domain into a certain finite number of volumes. In the centre of each of those volumes the quantity of each variable is calculated. In order to find a value for each variable at the volume surfaces interpolation between each centroid is used. Then the surface can be integrated and an algebraic equation for the control volume can be formed. Within these equations are also the values of neighbouring nodes [35]. In figure 14 an example of a 2D finite volume is illustrated.

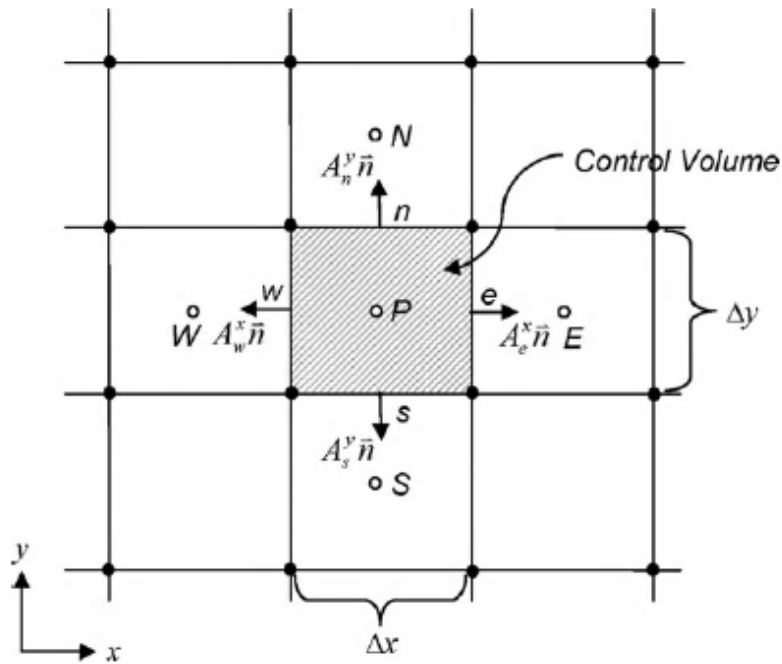


Figure 14: Example of a 2D control volume for the FVM [35]

2.4 Structural governing equations

The equations solved for the structural analysis are briefly presented here [25]. First the relationship between the force F and the displacement x is introduced for the static, linear case.

$$Kx_s = F \quad (2.28)$$

Here K is the stiffness matrix.

For the transient case the following equation is used:

$$M\ddot{x}_s + C\dot{x}_s + Kx_s = F(t) \quad (2.29)$$

Where M is the mass matrix, C the damping matrix and K the stiffness matrix. $F(t)$ represents the force vector which will vary with the time step, dependent on the flow around the wing. This relation can be simplified if it is assumed that the damping of the system is negligible. Here, it is assumed that force acting on the wing is much stronger than the influence of the damping from the air. Hence one can argue that the damping from the air can be considered negligible.

$$M\ddot{x}_s + Kx_s = F(t) \quad (2.30)$$

2.4.1 Finite Element Method (FEM)

For the structural case the FEM method is used to discretize the computational domain. Here the domain is divided into finite elements. Similar to FVM the method interpolates in order to calculate variables. However, a difference is that each variable is multiplied by a so called shape function before integration takes place. This can be expressed as:

$$\Phi = \sum_{j=1}^n \Phi_j \Psi_j(x, y, z) \quad (2.31)$$

Where Φ is an arbitrary variable, n represents the number of nodes, Φ_j , and Ψ the shape function [35]. For linear shape functions they can easily be constructed from the corner of each element. After multiplication with the shape function the approximated variable, Φ , is substituted into the integral of the weighted residual. The integral takes place over the entire domain with the expected result of zero. Making this substitution and integration creates a system of algebraic equations that can be solved numerically. In equation 2.32 this integration of the weighted residual with the weight function W_m and the equation residual R can be seen [35, 36].

$$\iiint_V W_m(x, y, z) R dx dy dz = 0 \quad (2.32)$$

2.5 Fluid Structure Interaction

The transfer of data between the fluid and structural solver differs depending on the problem one would like to solve. In this thesis the problem is considered isentropic, hence no heat transfer is considered, which leaves pressure and displacement. Pressure is transferred from the fluid solver to the structural- and displacement from the structural- to the fluid solver.

Within FSI there are different approaches that are used: the partitioned and the monolithic approach (see figure 15). The partitioned approach is more commonly used due to its integration

in commercial software but both of the approaches have their benefits and drawbacks.

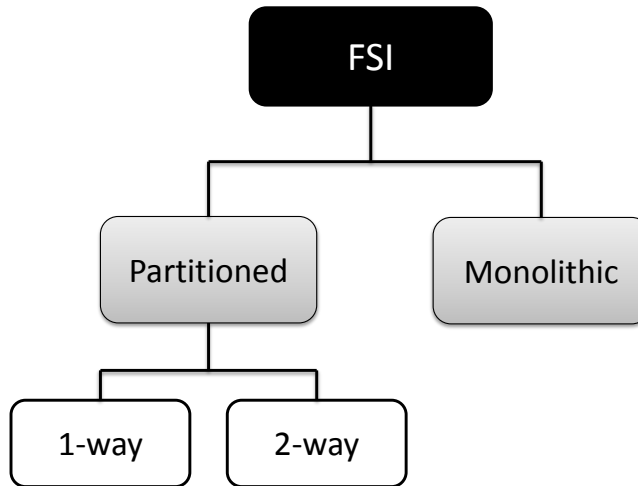


Figure 15: Different approaches for FSI

2.5.1 Monolithic approach

When fluid and solid equations are solved using a single matrix, hence making the system fully coupled, the approach is said to be monolithic. This approach is considered to be more stable and efficient. However, it is difficult to integrate optimal solvers for the fluid- and the mechanical part with a monolithic approach. For example, fluid solvers usually use FVM whereas structural solvers more commonly use FEM. In order to solve both the fluid- and the structural part of the simulation in one matrix one of the discretization schemes must be chosen. The monolithic approach also requires a conformal mesh between the structural and fluid solver which is not optimal for all cases [37].

2.5.2 Partitioned approach

In the partitioned approach each physical environment has its own solver; fluid solver for fluid simulation, structural solver for structural simulation. The results are transferred between the solvers via an interface, see figure 16. This gives the possibility to use state of the art software solvers and the opportunity to use non-conformal interfaces between structural and fluid meshes. However, the system is less efficient and tends to be less stable [38].

In a partitioned approach a mapping method is needed in order to transfer the loads between the fluid- and structural environment. There are many different ways of doing this [39, 38] and in this thesis two different approaches are used. For non-conservative quantities (e.g. displacement)

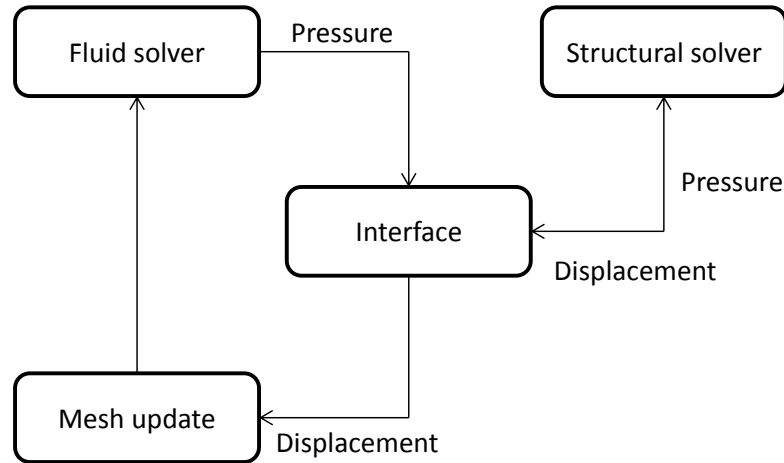


Figure 16: Data transfer for the partitioned approach

an algorithm called the Profile Preserving algorithm is used which uses the Bucket Mapping algorithm for mapping. In this mapping method the quantities are assumed not having to be globally conservative, but rather the shape of the surface should be conserved.

Conservative quantities (e.g. energy, momentum, force) use another mapping algorithm called General Grid Interface. This method calculates weights on the interface locally which conserves the quantities. If the mapping is done correctly all local quantities are fully conserved which means the global conservation is guaranteed as well [40].

The partitioned approach can be divided into a weakly- and a strongly coupled. The weakly coupled analysis has one data transfer in each time step whereas the strongly coupled analysis has multiple data transfers in each time step. This leads to a faster but less accurate simulation in the case of the weak coupling and the opposite for the strong coupling.

When using a partitioned approach it is also possible to conduct a one-way transfer analysis. An example of this is when deformation of a structure induced by a fluid are not considered large enough to affect the flow in a major way. This essentially means solving a fluid solver and transferring the pressure loads to a fluid structure interface as a boundary condition for a structural analysis [40].

2.5.3 FSI Governing Equations

The boundary conditions at the interface between the fluid and the structure are governed by kinematic condition

$$x_f = x_s \quad (2.33)$$

and the dynamic condition

$$\mathbf{n}_f \cdot \underline{\tau}_f = -\mathbf{n}_s \cdot \underline{\tau}_s \quad (2.34)$$

where x_f and x_s represent displacement for the fluid and structural interface, $\underline{\tau}_f$ and $\underline{\tau}_s$ is the stress tensor for the fluid and structural part and \mathbf{n}_f and \mathbf{n}_s the unit normal vector that points

outwards from the interface [39, 38].

The boundary condition of the velocity of the fluid on the interface is defined as the velocity of the structure at that point. Hence a no-slip boundary condition is still active (relative velocity between fluid at wall and wall is zero), but due to motion of the wing there will be a velocity of the wall itself. This can be described by the following equation,

$$u_w = \dot{x}_s \quad (2.35)$$

where u_w is the velocity of the fluid at the wall and \dot{x}_s the velocity of the the wall itself [39].

3 Method

In this chapter the method that was used in order to conduct the simulations is presented. First is a brief introduction of the software and the AWE system. After this comes the setup for the fluid and structural environment, followed by the setup for the FSI simulation. Three different approaches to simulate gust winds are presented after this, which is followed by a validation that contains grid convergence studies and a comparison between high fidelity and low fidelity results.

3.1 Software

The simulations are conducted with the ANSYS software package, version 17.0. The ANSYS package offers a variety of solvers, mesh generating software and post processing tools. ANSYS is widely used and recognized within industry and academic research and is considered state of the art both for mechanical- and fluid solvers [41].

The geometry- and mesh generation for the fluid environment is made with ANSYS ICEM CFD. The geometry- and mesh for the structural environment is part of the optimisation tool and not generated by the author. For the fluid environment ANSYS Fluent is used as solver and for the structural environment ANSYS Structural Mechanical is utilised. In order to couple the two solvers the software System Coupling is used. System coupling is a software that is made specifically for coupling ANSYS solvers.

3.2 AWE System

The AWE system that this thesis takes into consideration is of the Lift mode design and the wing flies in a circular pattern when generating power. In figure 17 the AWE system is illustrated.

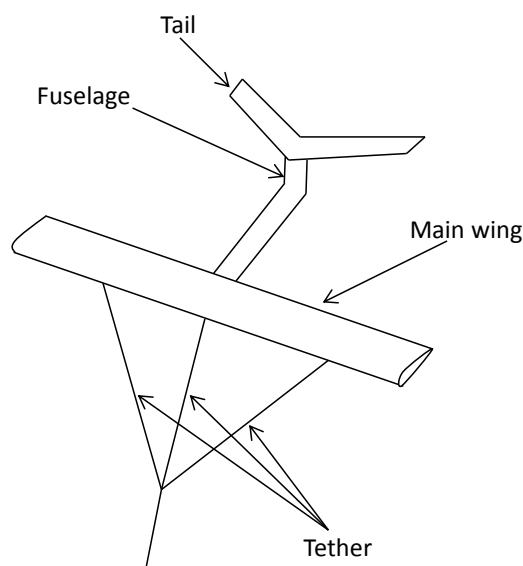


Figure 17: Schematic illustration of aircraft for AWE system

3.3 Fluid Environment Setup

3.3.1 Approximations

The flight is approximated as linear in the scope of this thesis. This means that the flow dynamics due to the circular flight pattern are not considered.

Only the semi-span of the main wing is simulated and in reality the flow is affected by the tethers and the tail of the aircraft. However, in the scope of this thesis, these effects are considered small enough to neglect. Furthermore the flow is considered incompressible.

3.3.2 Fluid geometry and mesh generation

In order to make the geometry- and mesh generation automated and robust they are both generated in ICEM CFD. By building the geometry from point data any wing geometry can be generated, assuming the same number of points exists on each airfoil, and the number of airfoils imported are the same. The automated generation is made with the scripting ability in ICEM CFD. Hence, all that is needed in order to generate a mesh for a new wing is to change the .dat file with the wing point data.

From the point data curves are generated, followed by surfaces. When the wing geometry is completed the fluid domain can be created in the same way. To make sure that the geometry is "watertight", the command Build Topology is used to close any existing gaps that might exist. Important to notice here is that tolerance can play a big part in how accurately the geometry is built. By keeping the tolerance too small, the risk of having unnecessary gaps increases. However, with a large tolerance certain features of the geometry might get lost.

A hexahedral mesh is used due to the many advantages in terms of CPU time and accuracy in comparison with tetrahedral meshes [35]. In order to generate the hexahedral mesh a multi-block approach is used. This means the fluid domain is divided into multiple blocks. The difficulty with this approach is to find a topology for the structure of the blocks that ensures high quality elements. The approach also requires some experience from the user which means it typically takes a longer time for an inexperienced user to generate a good quality mesh.

All blocks are filled with hexahedral cells with the exception of a small portion of the trailing edge at the wingtip. Due to the high angle, good quality hexahedral cells are not possible to generate, hence a block of swept unstructured cells (prisms) is generated instead. In figure 18 the surface mesh of the wing, the boundary layer mesh and the fluid domain is shown and in figure 19 the prisms on the wingtip are shown.

A separate fluid region, called Gust Region, is created upstream from the wing. The distance and size of this region can be specified by the user. This region is made to make it easier to add a source term later in the simulation process.

Lastly, the user has the possibility to coarsen the mesh in the spanwise direction in order to save nodes. Here the blocks closest to the wing geometry keep their original node distribution and the distribution of the blocks further away from the wing is divided with a factor of two. Keep in mind that ANSYS Fluent can handle 2 to 1 refinement interfaces for meshes, but other solvers might not be able to. In the case of this thesis the coarsening is made in order to save nodes.

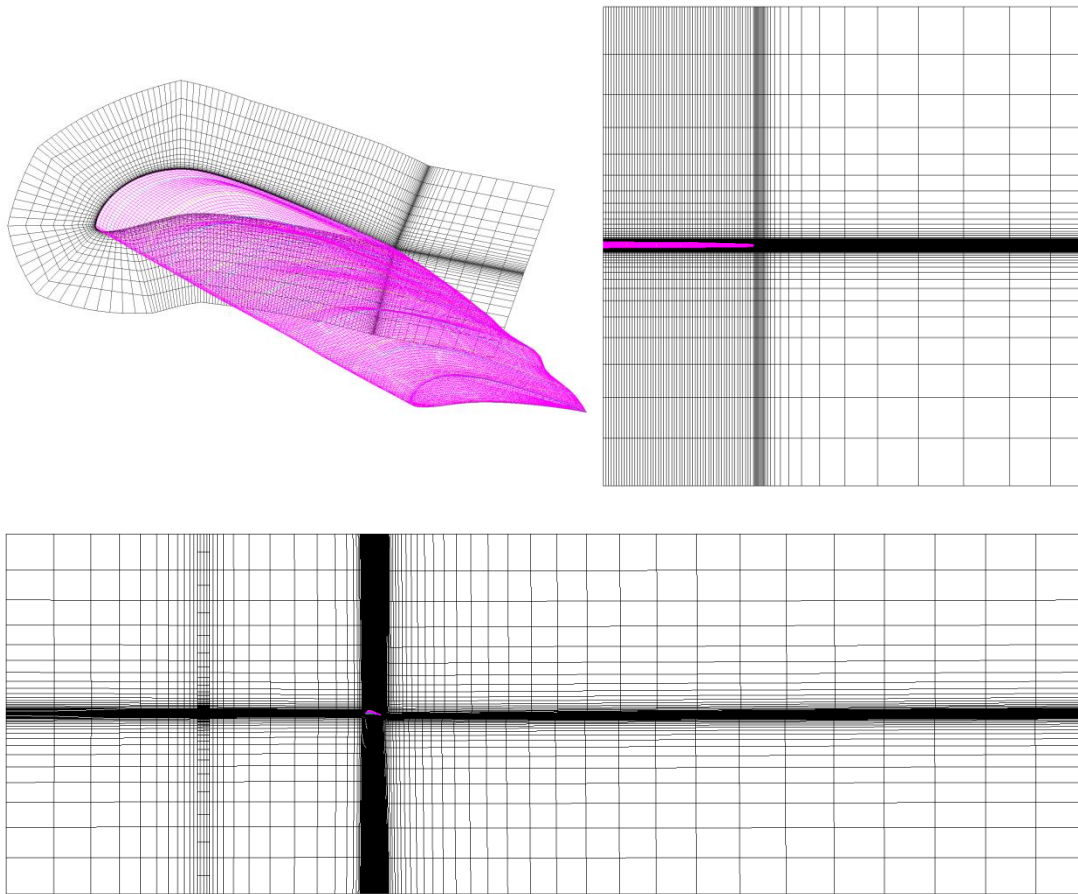


Figure 18: Top left: surface mesh of wing and boundary layer mesh, top right: front view fluid domain, down: side view domain

Because the geometry will differ slightly from wing to wing one should keep in mind that when importing point data for a new wing, some corrections might need to be done in the blocking. This can be done by stopping the script, rearranging the blocking, and letting the script continue until it finishes. The amount of nodes, wall distance, bunching laws etc. can be changed by the user after the script has run, or in the script directly.

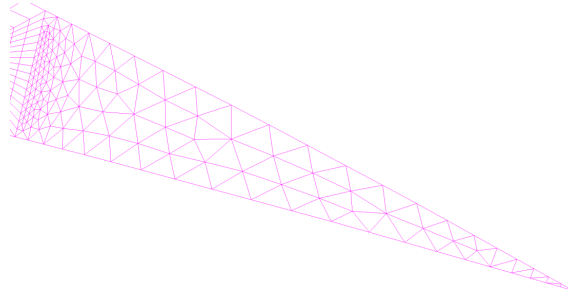


Figure 19: Prisms at wing tip

3.3.3 Boundary conditions and settings

The pressure based solver is used with the SIMPLE algorithm in order to couple pressure and velocity. The turbulence equations and the momentum equation are discretised with a second order upwind accuracy. For the pressure a general second order spatial discretization is used and for gradients the least squares cell based method is chosen. For the transient formula a second order implicit method is used.

The default under-relaxation factors that are used are presented in table 1.

Table 1: Under-relaxation factors

Pressure	0.3
Density	1
Body Forces	1
Momentum	0.7
Turb. Kin. Energy	0.8
Spec. Diss. Rate	0.8
Turb. Viscosity	1

In figure 20 and table 2 the boundary conditions are presented. u_i , u_j and u_k is the velocity in x-, y- and z-direction.

Table 2: Boundary conditions in fluid environment, (*) = u_i , u_j and u_k

velocity inlet	set inlet velocity [m/s]
pressure outlet	set gauge pressure [Pa]
slip-slip	$\tau = 0[N]$
symmetry	$d(*)/dx_k = u_k = 0[m/s^2]$
no-slip	$u_i = u_j = u_k = 0[m/s]$

The inlet velocity is a parameter used in the optimization and is set to 100 m/s for the final simulations. The gauge pressure in the outlet is set to 0 Pa.

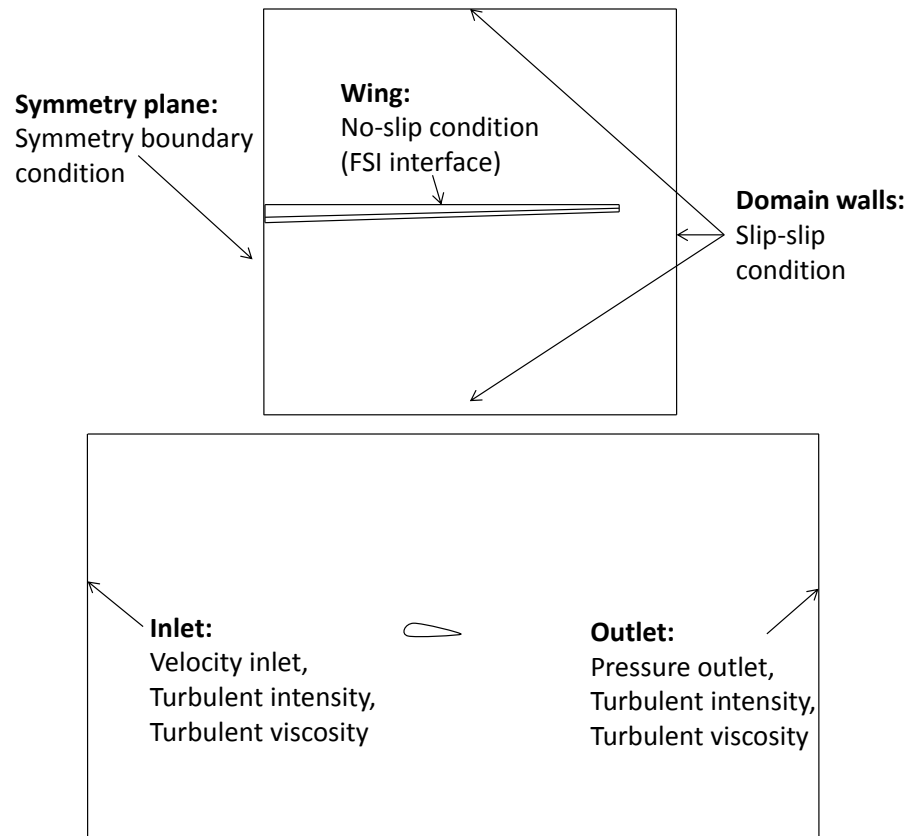


Figure 20: Boundary conditions in the fluid environment

Regarding the turbulence boundary conditions on the inlet and outlet they are set to follow the guidelines presented by Spalart and Rumsey [42].

3.4 Structural Environment Setup

3.4.1 Approximations

The structure in this thesis is approximated to behave linearly. The tethers attachment to the wing will cause the deformations to be considerably small in comparison to a case without a tether attachment. Due to the considerably small deformations this approximation is considered to be within reach for the scope of this thesis.

3.4.2 Wing Concept and Morphing Strategy

The morphing concept in this thesis was first presented by Molinari et. al [43]. It utilises ribs with a selectively compliant inner structure. By optimising the inner structure, the wing can withstand the high aerodynamic loads at the same time as being compliant enough to morph. The concept was further implemented by Fasel et. al [15] for AWE applications with the difference of the actuation system. Where Molinari used piezo elements to control the morphing, Fasel utilises electromechanical linear actuators.

The morphing attains variations of the local lift coefficient by morphing in the chordwise direction, thus changing the local camber. In order to achieve chordwise morphing without

loosing stiffness in the spanwise direction a corrugated flexible skin that is highly anisotropic in its stiffness is used. Furthermore the wing consists of nine ribs and nine actuators for each semi-wingspan.

The material used for the wing is Carbon Fiber Reinforced Plastic (CFRP) due to its anisotropy and favorable lightweight characteristics. The geometry and composite layup of the wing are products of an optimisation, presented in [15]. The generation of the geometry and the mesh for the structural part is an extension of the existing optimization tool, developed by Molinari. The objectives of the research project is presented in section 1.1. Hence no further presentation of the generation of the structural geometry and mesh, nor the optimization is made. For further information about the optimization the reader is referred to [15].

3.4.3 Structural geometry and mesh

The final geometry and its mesh can be seen in figure 21.

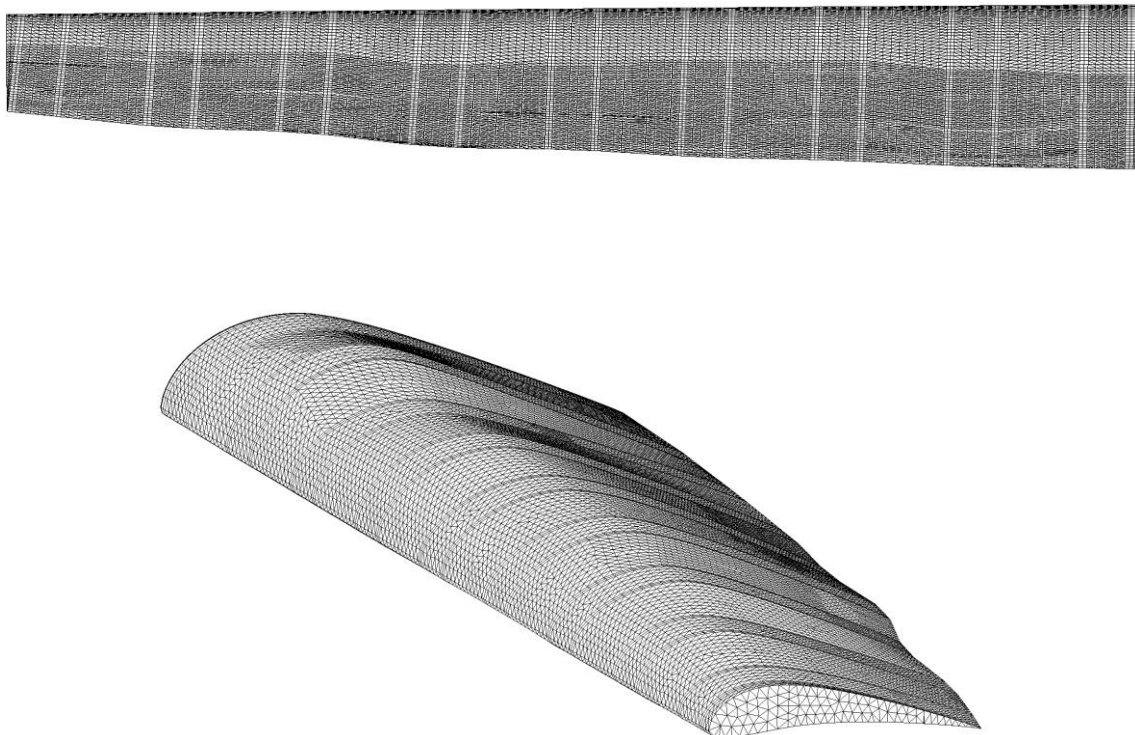


Figure 21: Structural mesh

As expected the wing is highly cambered in order to increase the lift force acting on it. As can be seen the airfoils differ along the wing span, both in camber and chord length. An unstructured

shell mesh is used for the structural part making the automatic generation of a high quality mesh easier for the complex inner structure.

3.4.4 Structural boundary conditions

The semispan of the wing is simulated and the root of the wing is fixed to the symmetry plane with zero degrees of freedom. The tether connected to the wing is simulated as a rod element fixed to symmetry plane as well, with zero degrees of freedom. In figure 22 the boundary conditions are shown in a schematic illustration.

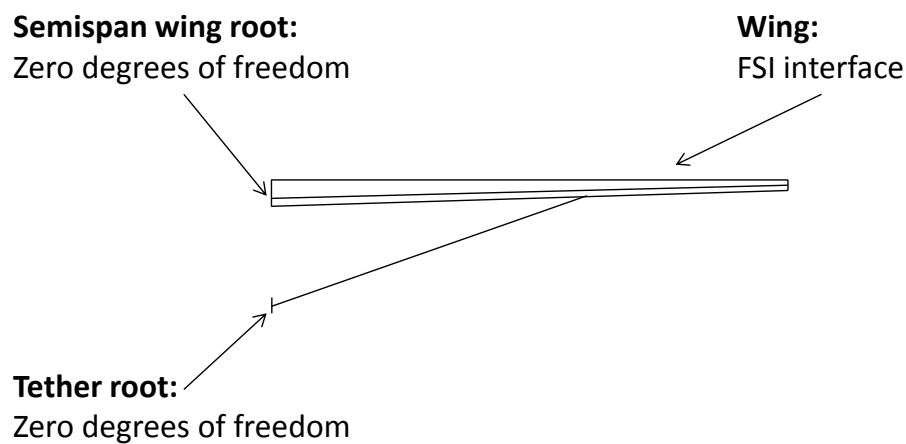


Figure 22: Boundary conditions for structural environment

The morphing is simulated by having rod elements acting as linear actuators. This is done with temperature boundary conditions that causes the rod element to elongate or shorten as the linear actuator would do in reality. This is illustrated in figure 23.

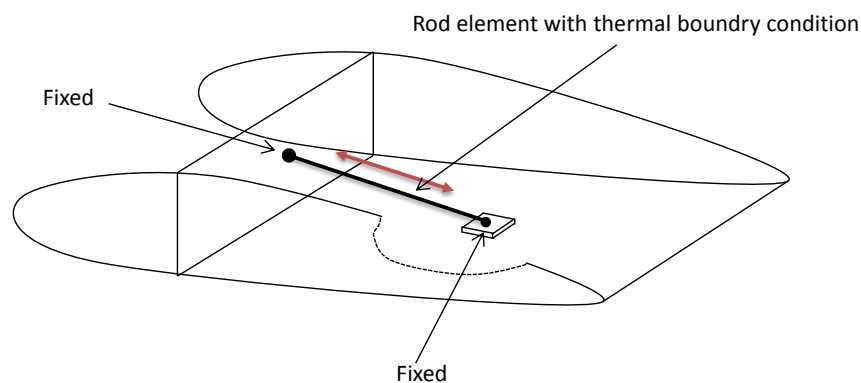


Figure 23: Thermal boundary condition for actuation

3.5 Fluid Structure Interaction Setup

3.5.1 FSI overview and co-simulation sequencing

Two different approaches can be chosen for the solving process; Sequential Solutions and Simultaneous Solutions. The simultaneous solution gives the different solvers the same sequential solver values. In the sequential alternative the solvers are engaged in a certain order, specified by the user. The sequential Solutions are typically used for strongly coupled problems [40]. Here the sequential alternative is used with the ANSYS Transient Analysis the simulation (receiving pressure loads from ANYSY Fluent). In figure 24 the overview of the FSI setup is shown.

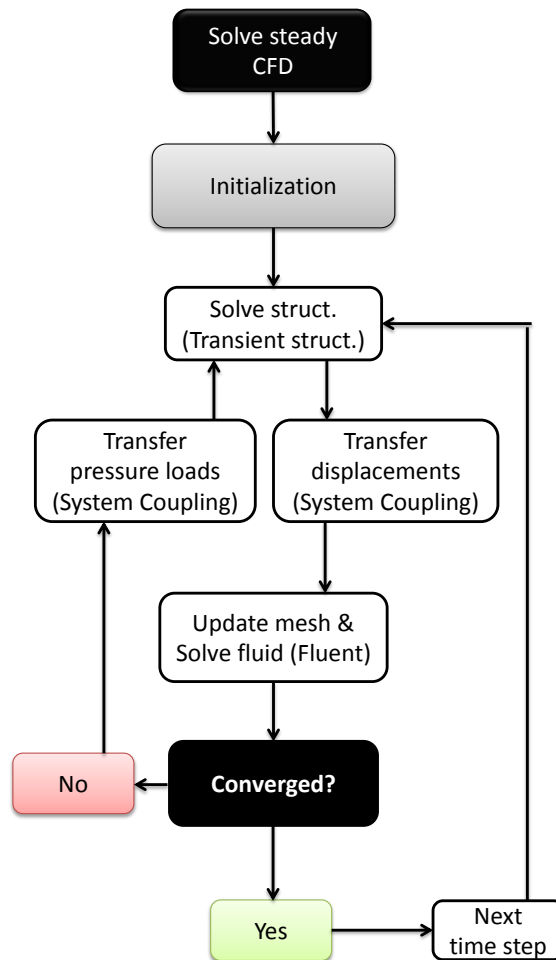


Figure 24: Overview of FSI

3.5.2 Initialization

Steady state FSI is not available when coupling Fluent and Structural Transient with System Coupling. Instead the simulation is initialized with a steady state fluid simulation. This transfers to the mechanical solver and starts the coupled simulation. The problem with this approach is that a large force hits the wing in a short time in the beginning of the simulation (depending on the time step). For an elastic structure this can lead to large deformations and oscillations that takes a long time to smooth out. Additionally, this can lead to negative cell volumes in Fluent due to larger deformations than the dynamic mesh can handle.

3.5.3 Solution Stabilization

Another difficulty with the coupling in this simulation is large deformations in combination with an incompressible flow. This can cause the solution to diverge which usually happens in the first few iterations. The reason for this instability can be explained by large changes in pressure in the fluid solver caused by the deformation in the structural solver. This might cause the deformations to increase which in turn would increase the pressure differences eventually causing the simulation to crash.

Fluent has a feature called Solution Stabilization in order to make the simulation more stable. One has to be careful however not to over stabilize the simulation, causing convergence to take a long time. A solution stabilization of 0.5 worked well for the simulations in this thesis.

3.5.4 Dynamic meshing

Fluent offers a dynamic mesh which has the ability to both smooth and remesh the fluid mesh. In the case of the morphing wing the deformations are expected to be small enough to only use the smoothing feature. Hence an approach without remeshing is considered.

Three different smoothing methods are available: spring-based smoothing, diffusion based smoothing and Linearly elastic solid smoothing. The spring based smoothing is not recommended for hexahedral cells and the linearly elastic solid method tends to be demanding in terms of computational effort. With this in mind the diffusion based smoothing method is used. One can choose from using the diffusion based smoothing method as a function of distance to the moving boundary or the volume of elements. Here the boundary distance is used. It is possible to control how much of the smoothing should take place far away or close to the moving boundary by setting a coefficient. Here a value of 2 is chosen for the coefficient.

More detail about the theory behind the diffusion based smoothing can be found in appendix A.

3.6 Gust simulation

The investigation of an appropriate method to simulate the gust wind is made within the fluid environment. By studying a number of different methods to simulate a gust wind, the different approaches can be validated and the most appropriate one can be selected. Three possible methods are selected for validation. The three approaches are picked based on three factors.

- Flexibility in terms of gust shape
- Flexibility in terms of gust duration
- Robustness

The importance of these factors comes down to the final simulation and the idea to control the morphing of the wing with a predetermined motion, rather than momentarily control the wing, dependent on how the wind gust appears. With this in mind it is important to be able to predict how the wind gust behaves in terms of shape and duration. In order to be able to simulate different gust scenarios the flexibility is important. For future use it is important that the implementation is robust and does not depend much on the user. For all the gust simulations the

cells surrounding the wing has a Courant number below 20 except for some cells at the wingtip and after the trailing edge of the wing. Because an implicit formulation is used and the solution converges this is considered a sufficient size of the Courant number.

All of the gust simulations are implemented with the help of user defined functions (UDF) in Fluent. For the approaches that uses momentum source terms, these are added as a cell zone condition. The region where they are added is created in the mesh generation process.

The specifications of the implementation of the UDFs can be found in appendix B.

3.6.1 Artificial duct

The first implementation considered is referred to as the artificial duct [44]. By defining a small region in the upper and lower boundaries of the domain as inlets followed by outlets that are moving over the domain, an artificial duct can be created. This is best understood through figure 25 where the idea is thoroughly illustrated. The flow is accelerated in the centre of the domain and the gust can be transferred over the domain.

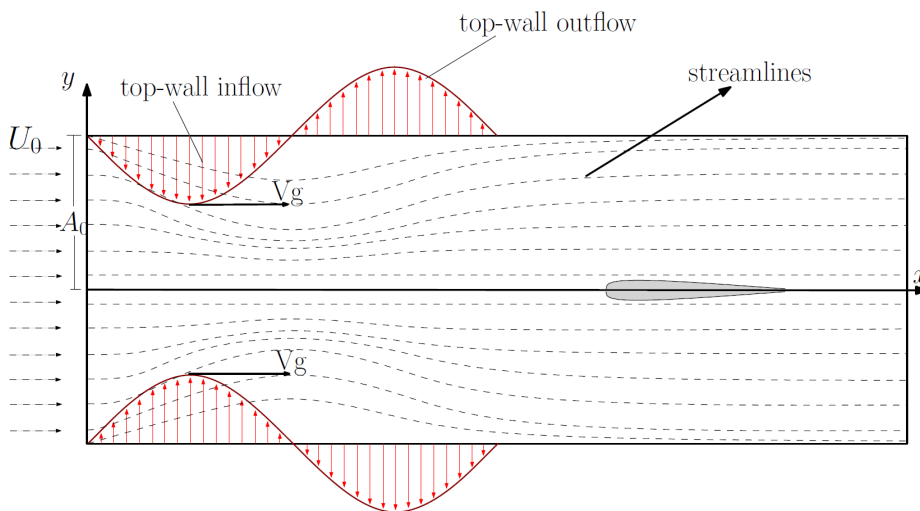


Figure 25: Moving inlet- and outlet boundary conditions on boundaries [44]

After implementation it was found troublesome to predetermine the shape and duration of the gust. The gust behaves best if it travels with the same velocity as the free stream velocity. If the free stream has a higher velocity than the moving boundary conditions, the higher velocity in the duct is partly transferred downstream of the domain via convection - leaving the gust to be less predictable. However, for high velocities the size of the moving inlet and outlets would be needed to become excessively large. This is best explained with an example: a gust with a duration of 10 seconds with a free stream of 100 m/s would need a gust length of 1000 m. Moreover the shape of the gust is difficult to change and predict. With this in mind this method is not chosen and not further discussed in the thesis.

3.6.2 Vortex based momentum source term

By increasing the vorticity in a region in front of the wing, a perturbation of the velocity can be convected downstream of the domain and hit the wing. This method was first used by David P. Lockard and Philip J. Morris [45], and later expanded for use in two dimension by Vladimir V. Golubev et. al. [46, 47, 48]. The theory behind the source term is thoroughly explained in [48].

The simulation results shows something similar to atmospheric turbulence, see figure 26. These flow conditions are of course interesting but does not really go in line with the goal of this thesis where a discrete gust simulation is to be simulated. It is also complex to change the shape and duration of the gust winds which could lead to a less robust method. With this in mind this method is not chosen and not further discussed in the thesis.

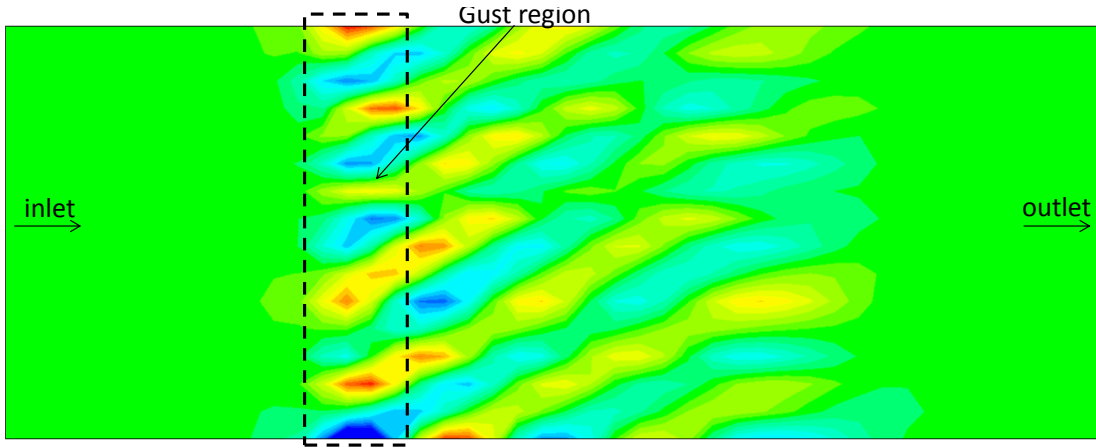


Figure 26: Velocity field of the domain with vortex based source term

3.6.3 Forcing momentum source term

The final implementation is also the one deemed the best alternative for the purpose of this thesis. The method is based on implementing a momentum source term. This source term forces the velocity in this region to a certain amplitude. The flow with the forced velocity then travels downstream through convection and hits the wing. Because of numerical diffusion the magnitude of the velocity will become a little damped further downstream from the source region. However, the source region can be located at a distance not far from the wing, minimising the effect of numerical diffusion.

The idea of implementing a gust that travels downstream via convection is not new [49]. For example Golubev et. al. used it to model sharp gusts for micro-air vehicles by implementing a momentum source term with constant velocity perturbations [46]. In this thesis, however, the idea is to use time varying velocity perturbations in the source term in order to be able to change the nature of the gust.

The source term acts in a way so that it goes towards zero as the velocity within the source region approaches the forced velocity as can be seen in equation 3.1.

$$S = (u_{forced} - u_{current}) \frac{B}{dt} \quad (3.1)$$

Here $u_{current}$ is the variable that is updated between the iterations and u_{forced} is the velocity that is aspired. As can be seen the source term disappears when $u_{current} = u_{forced}$, leading to

the solutions convergence. B is a constant and dt is the size of the time step. These terms work in order to keep the right units for the momentum source term and accelerate the convergence if needed. This gives for a flexible gust simulation. Any geometrical function can be assigned to u_{forced} and the velocity in the source region will be forced to the shape of this function. Notice that for a smaller time step the ratio B/dt becomes larger. This should be taken into consideration if the time step of the simulation is changed.

When adding momentum in a region that covers the entire cross section one runs the risk of creating a pressure wave. The pressure wave comes from the added momentum that pushes the flow downstream. An analogy can be made with a wave machine in a pool with an outlet and an inlet. If a force is added at the inlet of the pool it will create a wave that will travel from the inlet to the outlet. However, if the entire pool would get the same amount of force at the same time no wave would be created but the entire flow would accelerate. This can be translated as having a region where the momentum is added upstream, or adding the momentum in the entire domain. However, adding the momentum in the entire domain would decrease the influence that the wing would have on the gust wind. This is because the velocity in the entire domain would be forced to a certain magnitude at the beginning of each time step. By adding a source region upstream it is possible to let the gust travel downstream and interact with the wing naturally.

In order to reduce the effect of the pressure wave a region next to the wall facing the tip of the wing is left without any added momentum. The velocity of this region is reduced due to the changes of pressure through out the domain. The pressure wave will most likely be larger for smaller time steps. The reason for this is that the momentum is added during a smaller time. This means a larger pressure gradient, leading to a larger pressure wave through out the domain. Hence, a larger time step will lead to a smoother implementation.

In figure 27 the gust simulation is shown where T represents the normalized time. This can be compared with figure 28 where the normalized lift and the normalized velocity for the same simulation is plotted and the snap shots in figure 27 are marked out.

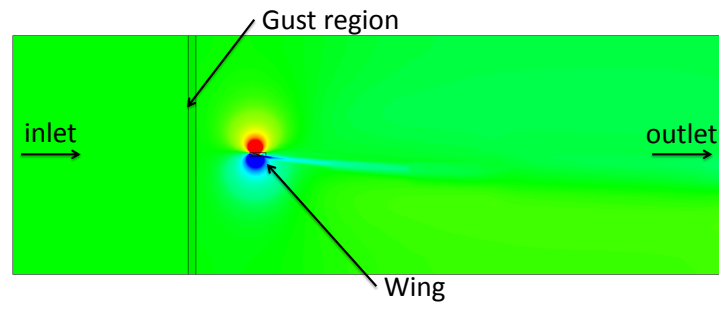
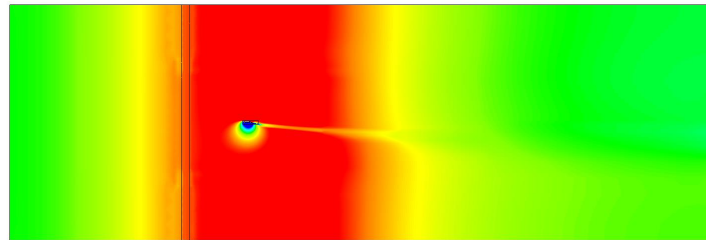
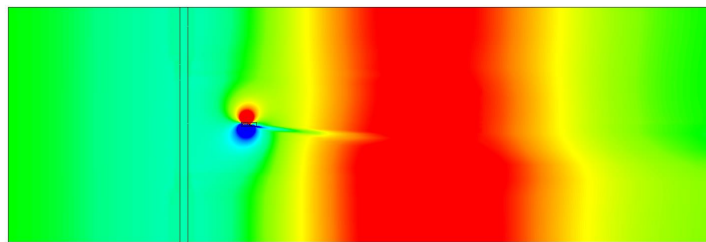
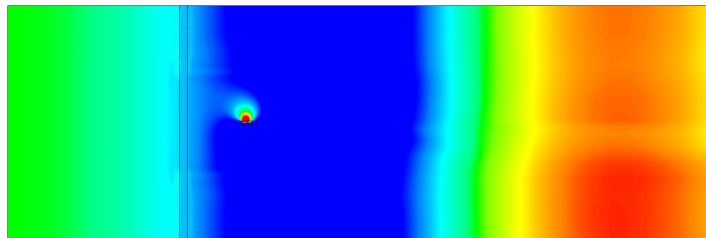
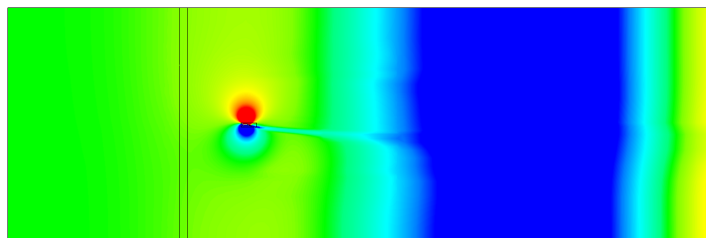
(a) $T = 0$ (b) $T = 1/4$ (c) $T = 2/4$ (d) $T = 3/4$ (e) $T = 4/4$

Figure 27: Gust with sinusoidal shape, amp. of 5 m/s

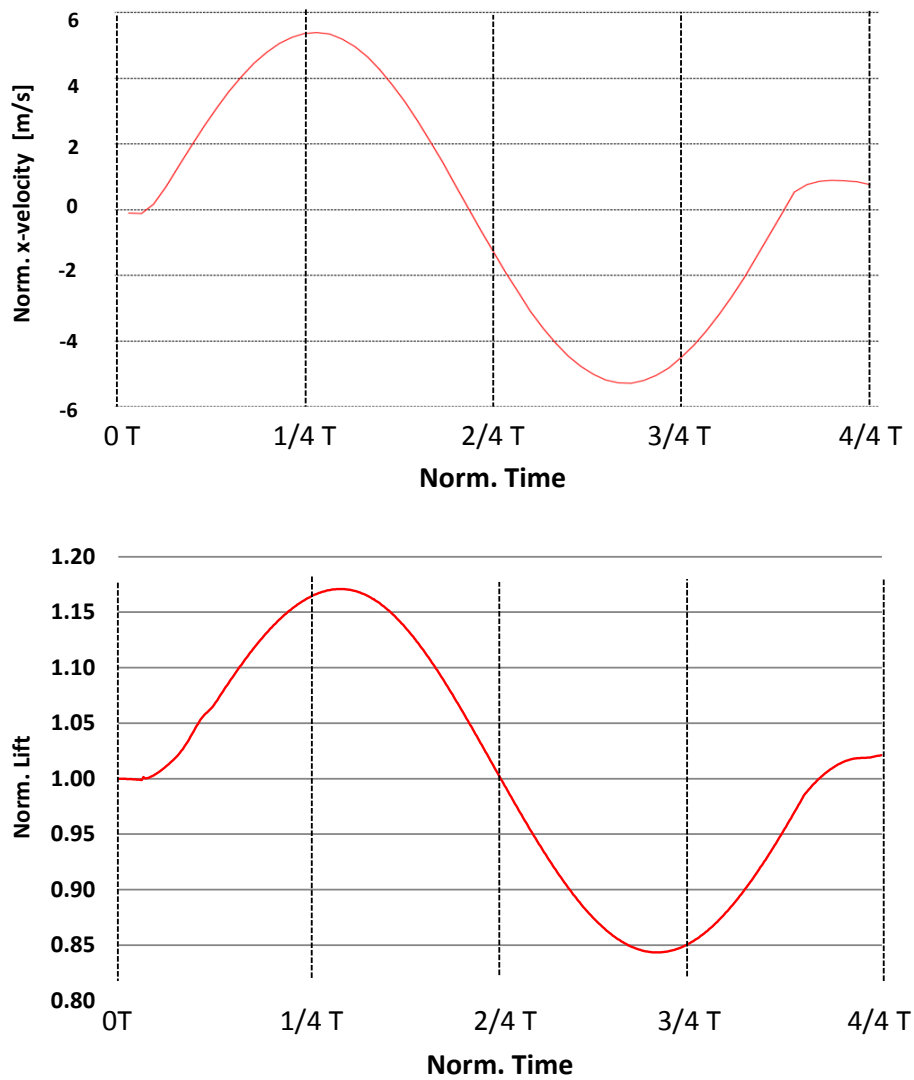


Figure 28: Normalized lift and velocity as a function of the normalized time

3.7 Validation

3.7.1 Grid convergence study

Considering that different wings will be used in the future, a generic convergence study with a generic wing is carried out. The wing, NACA0012, is chosen based on the many experiments that has been carried out on it. This makes it possible to compare the results in the grid convergence study not only with themselves, but also with experimental data for validation.

The data used for validation originates from experiments conducted by Applin in 1995 [50]. Here pressure data over the wing is presented for a Reynolds number of $5e6$. The data was later converted into a plot with C_l and C_d as a function of AoA by D. Bruce Owens in 1998 [51]. With this in mind the convergence study is made with a Reynolds number of $5e6$ and an AoA of 5 degrees and the results are compared with the plot in [51]. Furthermore a similar

Reynolds number is expected in the case of the AWE wing meaning it gives a good idea of the grid resolution required for simulations of AWE wings in the future. In table 3 the boundary conditions for the grid convergence study are presented. The dimensions of the wing is a chord of 0.6 m and a semi-span of 1.71 m.

Table 3: Boundary conditions for grid convergence study

Inlet	$u = 114.7 \text{ m/s}$
Outlet	$p = 0 \text{ Pa}$

In the convergence study four different cases are considered. The refinement focuses on the area surrounding the wing, whereas regions further away keep a more static cell size. This is because high gradients are only expected to exist close to the wing. These results are presented in table 4 and in figure 29 a plot of the results are shown.

Table 4: C_L and C_D in convergence study

	C_L	C_D
Coarse	0.35799	0.01672
Medium	0.36552	0.01674
Fine	0.36647	0.01661
Very fine	0.36721	0.01660
Rich. Ext.	0.36744	0.01660
Experiment	0.35	0.0164

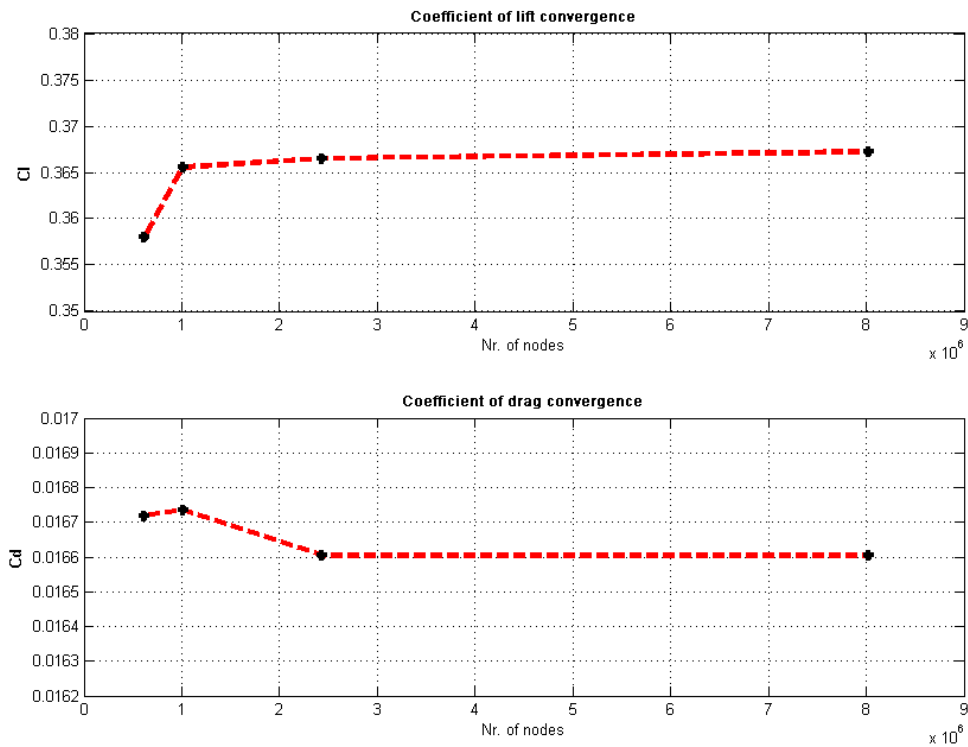


Figure 29: C_L and C_D in convergence study

A sensitivity study in terms of turbulence model and wall treatment is considered for the final mesh size. Three different turbulence models that are all common in aerospace applications are

compared: Spalart-Allmaras, K-omega SST and K-omega SST transitional. For K-omega SST transitional a y_+ of 1 or less is considered, K-omega SST is analysed for y_+ of 1 and for wall-functions. For Spalart-Allmaras only the wall function approach is considered. The results of this study are shown in table 5.

Table 5: Different turbulence models for medium size mesh

	C_L	C_D
K-omega SST	0.36552	0.01674
Transitional	0.36814	0.01572
Wall func. K-omega SST	0.36637	0.01671
Wall func. Spalart Almares	0.37092	0.01723
Rich. Ext.	0.36744	0.01660
Experiment	0.35	0.0164

Included in the convergence study is also a verification that the domain is large enough, and does not affect the solution. Here two cases are made, one large domain and one small domain. The grid convergence study regarding the size of the mesh is conducted on the large domain. The result of the final mesh size is then analysed for the two different domain sizes. The dimensions are presented in table 6 as distances from point $x=y=z=0$ (0,0,0) which is approximately where the leading edge of the wing is located at the symmetry plane.

Table 6: Domain sizes, (0,0,0) indicates point $x=y=z=0$

(0,0,0) - inlet	15 m	10 m
(0,0,0) - outlet	30 m	20 m
(0,0,0) - wall side	7.5 m	5 m
(0,0,0) - wall down	7.5 m	5 m
(0,0,0) - wall side	15 m	10 m

The results of the domain size influence are shown in table 7.

Table 7: C_L and C_D for medium sized mesh with large and small domain

	C_L	C_D
Small	0.36765	0.01667
Large	0.36552	0.01674
Difference	0.3516%	0.2469%

Based on the grid convergence study using the medium sized mesh is accurate enough as the results are well within 1% of the Richardson extrapolation for both coefficient of lift and -drag. The close relation to the experimental results is also worth noticing. The medium sized mesh has an approximate cell size of 1 cm in chord wise direction and max size of 10 cm in span wise direction. The y_+ is below 1 over the entire wing. The results of the sensitivity- and wall treatment study suggests that using the K-omega SST with wall functions for the medium sized mesh provides accurate enough results as well. Concerning the domain size the large domain is sufficient. The smaller domain is not chosen due to the small benefits it provides: the amount of nodes saved are not many enough to make a large difference in computational effort and with a larger domain, a wing that is larger in wingspan could be considered for this domain as well.

With the results in mind, using the large domain with medium mesh size and wall-functions is

the best compromise between accuracy and computational effort and is therefore chosen for the continuation of the thesis.

3.7.2 Investigation for final wing

An investigation of the influence of the y^+ and influence of chordwise cell size is conducted for the final wing. This is motivated by the difference in shape between the optimised wing and the NACA0012. A cell size of 0.05 m in chord wise direction and a y^+ of around 1 to fully resolve the viscous boundary layer is compared to a case with a cell size of 0.01 m in chord wise direction and a y^+ above 30, using wall functions. The cell size in chord wise direction is based on the previous grid convergence study where the results showed a chord wise cell size of 0.01 m is accurate enough. For the final wing the inlet velocity is changed to 100 m/s and for this comparison an AoA of 6 degrees is used. In table 8 the normalized results are shown.

Table 8: Normalized C_L and C_D for fully resolved- and wall function approach

	C_L	C_D
Fully resolved	1	1
Wall functions	0.98541	1.00746

As expected the finer mesh shows a slightly higher C_L and a slightly lower C_D . However, the results shows a difference of less than 2% for C_L and less than 1% for C_D . Hence the approach with wall functions and a chord wise cell size of 0.01 m is chosen for the rest of the simulations.

3.7.3 FSI comparison with low fidelity results

A comparison with low-fidelity results from the optimization tool, mentioned in the introduction, is made for an AoA of 6 degrees for the fluid structure interaction. The results are shown in table 9.

Table 9: Comparison between high-fidelity and low-fidelity results at AoA of 6 degrees

	C_L	C_D
Lo-Fi	1	1
Hi-Fi	0.8546	0.8769

The results shows a smaller lift and drag force for the high fidelity simulation in comparison to the low fidelity results. The reason for this is explained by 3D- and transient effects that the high-fidelity simulation takes into account, also discussed in the motivation for the thesis.

4 Results and discussion

In this chapter, the results from the FSI simulations are presented. First, the flow around the wingtip is shown. This is followed by the displacements of the wing at different points. The points are located at the leading- and trailing edge at three distances along the wingspan: at the wingtip, at the tether attachment and between the root and the tether attachment.

The results shows three different cases with gust interaction and actuation. A reference case is shown where the gust hits the wing with no actuation. The gust is added at 0.9 seconds and is simulated with an amplitude of 5 m/s and a duration of 0.5 seconds.

The three different cases consist of different actuation strategies, where the temperature boundary condition controlling the actuation differs with 20% for each case. The actuation will be strongest for the case with the highest temperature. From case 1 to case 3 the actuation gets stronger.

All cases interact with the same gust wind and each case starts actuating 0.1 seconds after the gust simulation starts.

4.1 Flow at wingtip

Figure 30 shows wing tip vortices appearing at the wingtip of the wing. These are the sources of induced drag. In order to reduce this, a wingtip device can be used. However, the use of a wingtip device will increase the area normal to the velocity of the wind which will lead to an increased profile drag. Furthermore, the weight of the wing will increase with the addition of wingtip devices. Further investigation must be done in order to conclude whether wingtip devices are a good addition for the AWE wing.

Another strategy to reduce the induced drag would be to change the shape of the wingtip. As mentioned in section 2.1 an elliptic shape of a wing is optimal in order to reduce induced drag. The aspect ratio of the wing also has a large influence. With this in mind a more elliptic shape or a decreased chord length of the wingtip could potentially reduce the induced drag.

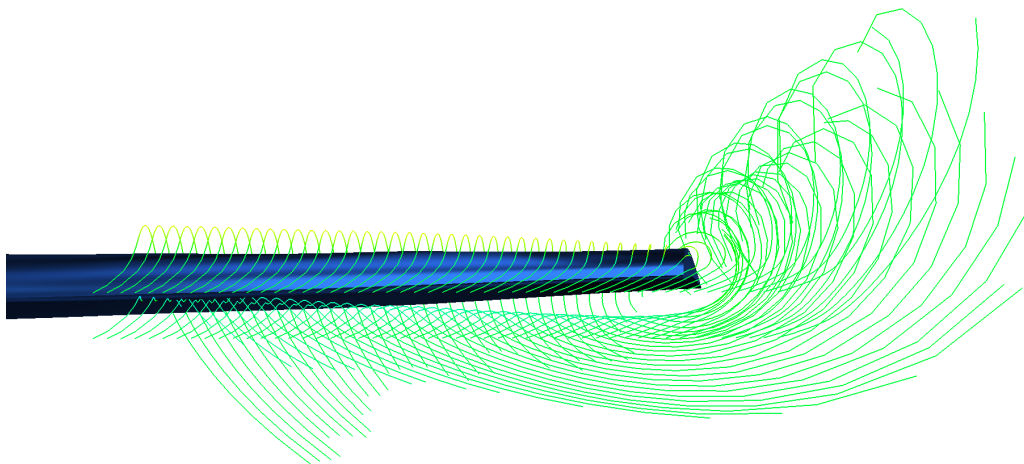


Figure 30: Wingtip vortex in simulation

At the wingtip a recirculation zone appeared, illustrated in figure 31. This is due to the sharp edge at the wingtip. Because of this the flow cannot follow the surface and separates. Here the wingtip could be shaped into a rounder, more aerodynamic shape. This would decrease the risk of separation at the wingtip and potentially improve the aerodynamic performance.

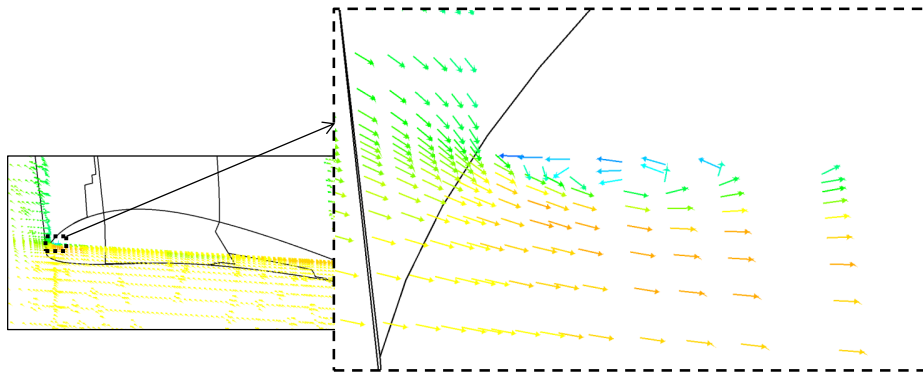


Figure 31: Recirculation at wingtip

4.2 Displacement

As can be seen in figure 32, the displacements are considerably larger at the wingtip in comparison to the tether attachment and more towards inner part of the wing. The tether is holding the displacements back leaving only the outer part of the wing free to oscillate with larger motion.

At the beginning of the simulation the oscillations are large and they gradually decrease with time. This is expected due to the sudden impact of the pressure forces from the fluid. After a while the large deformations smooth out, indicating that the wing will reach an equilibrium where the oscillations no longer decrease, nor expand. This indicates that the flutter speed of the wing is not reached with 100 m/s. However, in order to conclude this a full flutter analysis should be made.

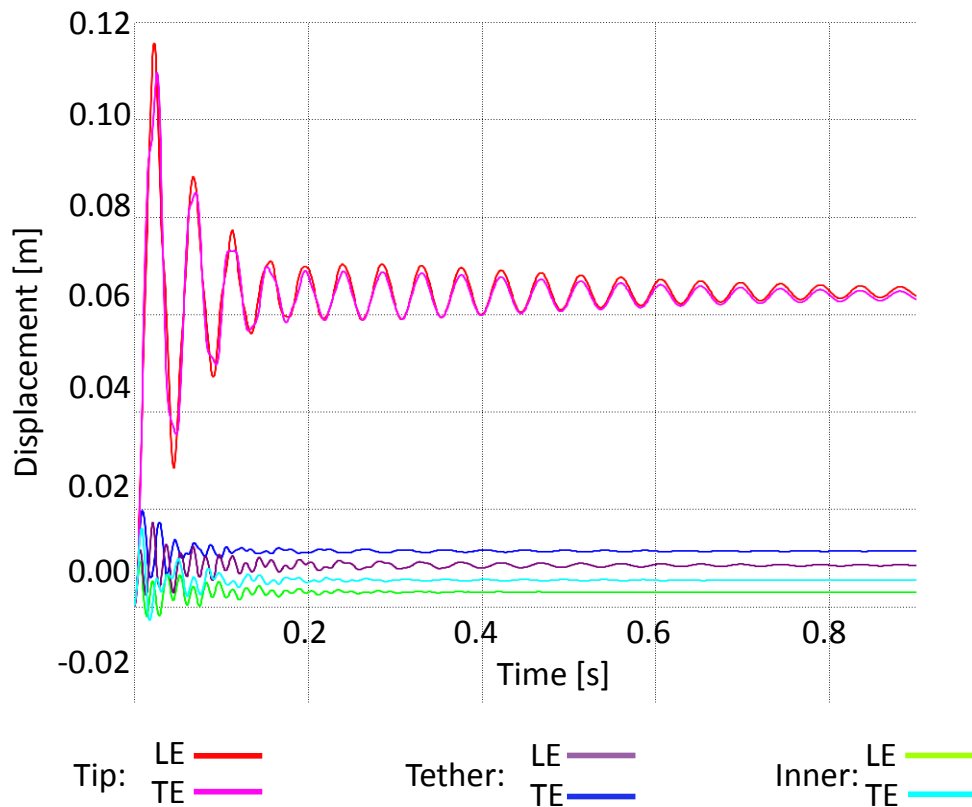


Figure 32: Displacement for gust interaction with no actuation

Figure 33, 34, 35, 36 shows the displacement for the different actuation cases, including the reference case with no actuation. The displacement is shown at the time where the gust interaction starts and continues until the gust has passed the wing .

Firstly it can be noted that when the gust hits the wing the overall displacements increase, but the oscillations continue to decrease for all cases. For the cases which use stronger actuation the displacements decrease more at the end of the gust. This is expected due to the decrease in lift force due to the actuation, which is followed by a smaller displacement in the positive y-direction.

It seems that that actuation itself is rather small in comparison to the general movement of the wing. This implies that small changes in the geometry can lead to a relatively large load alleviation.

It can be seen that the displacements for the points at the tether attachment and further towards the wingtip starts to behave differently at the second half of the gust simulation. This is explained by separation occurring locally on the wing. When the actuation becomes stronger the camber on the wingtip decreases. However, the morphing can lead to local increase in camber at other places of the wing. At a certain actuation the deformation of the wing causes the flow to separate locally which explains the unstructured displacement pattern for case 3.

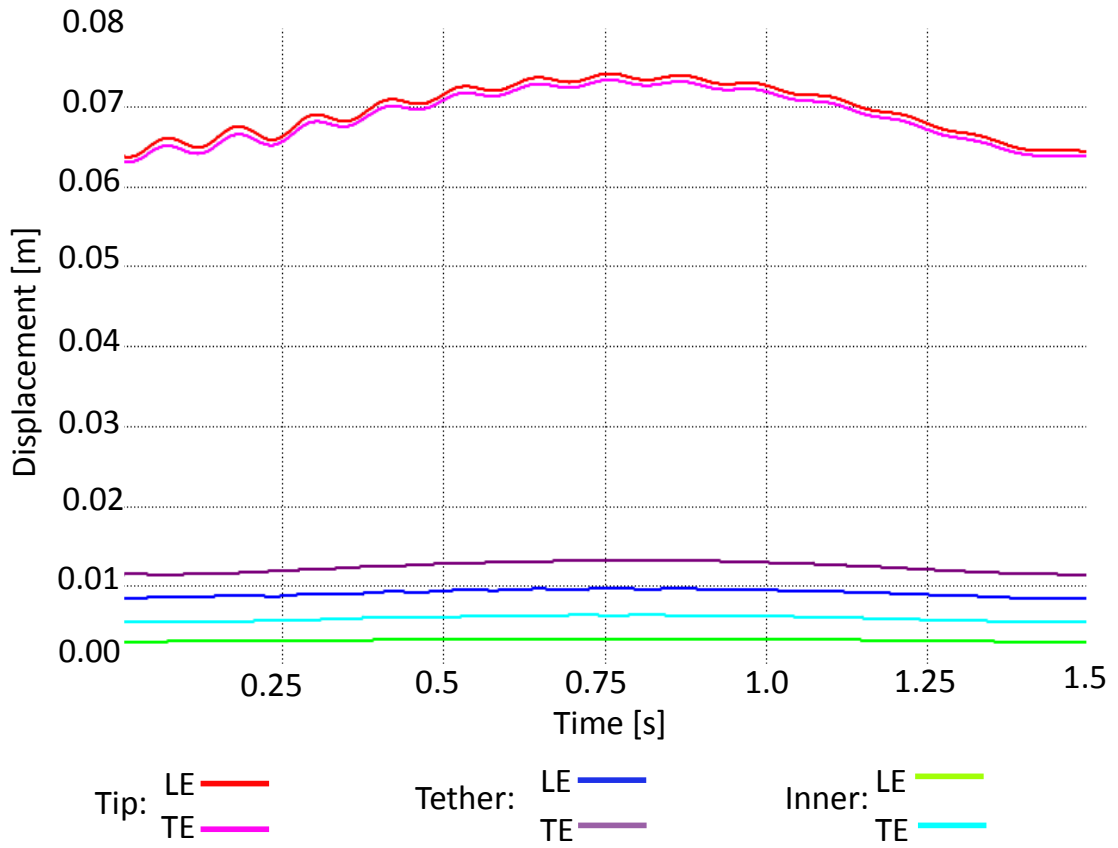


Figure 33: Displacement during gust interaction with no actuation

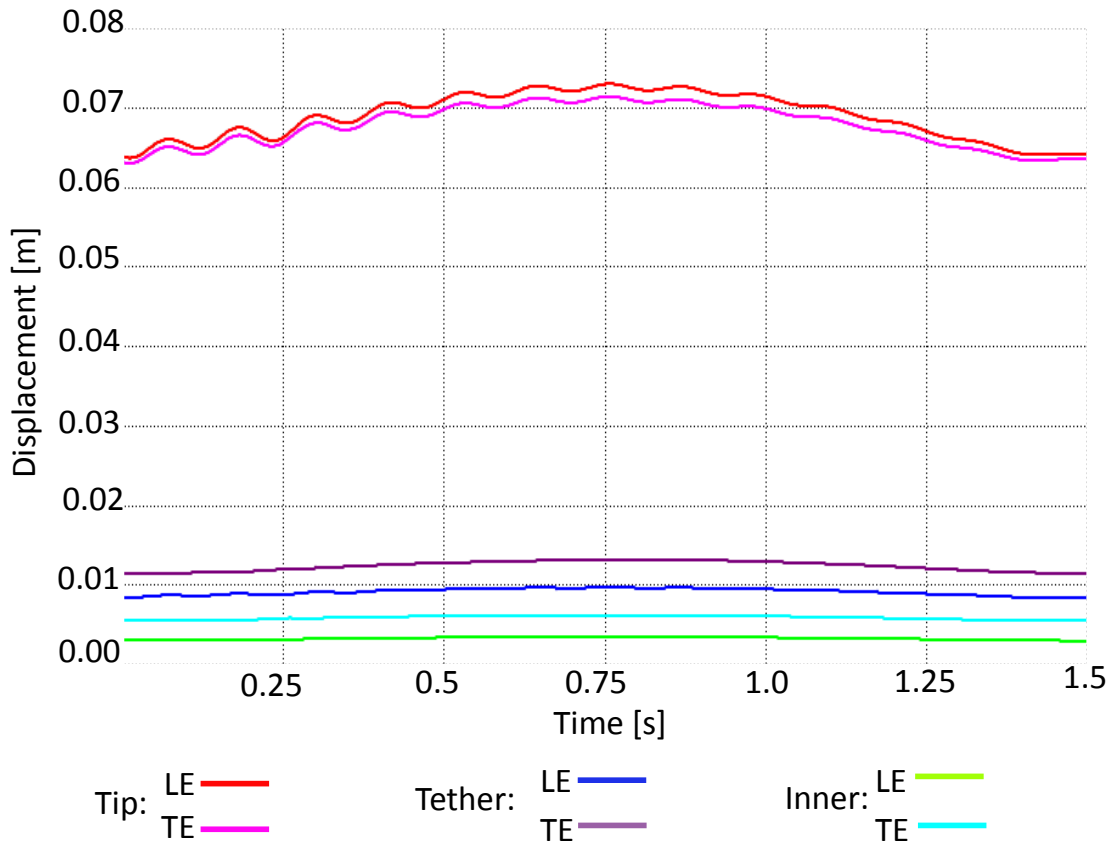


Figure 34: Displacement during gust interaction for case 1 actuation

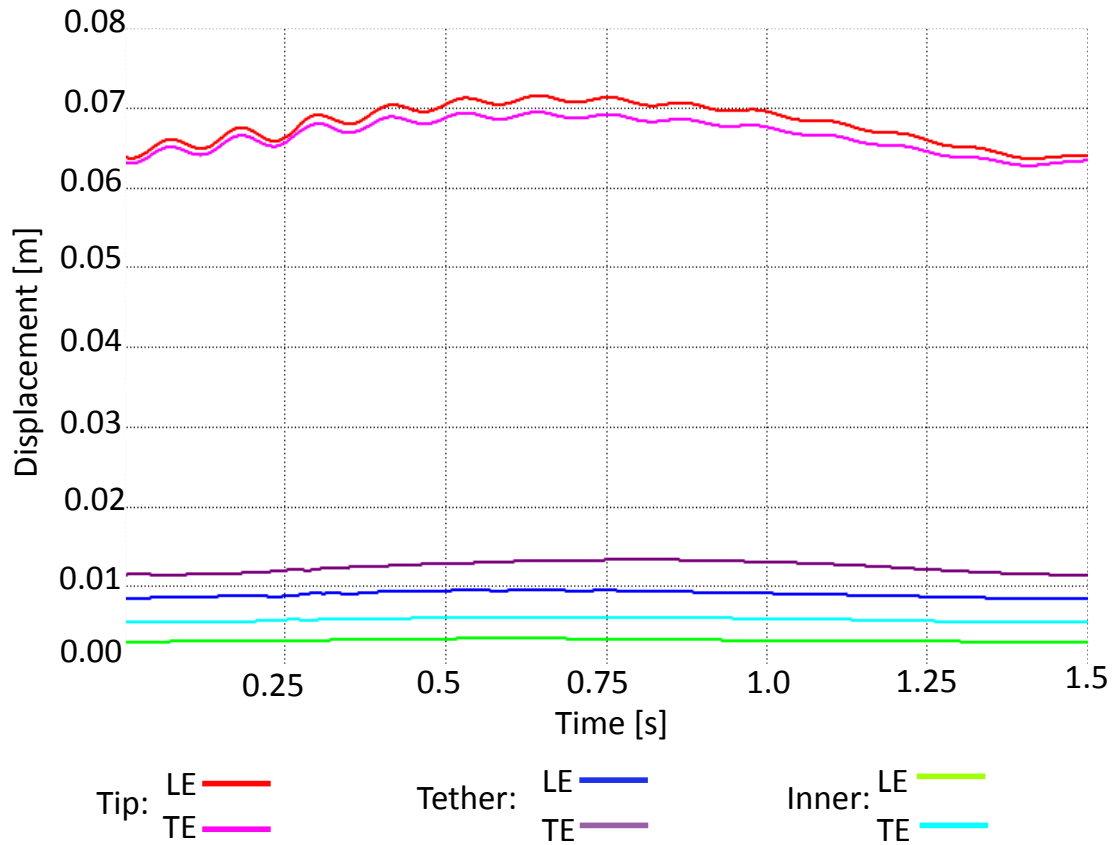


Figure 35: Displacement during gust interaction for case 2 actuation

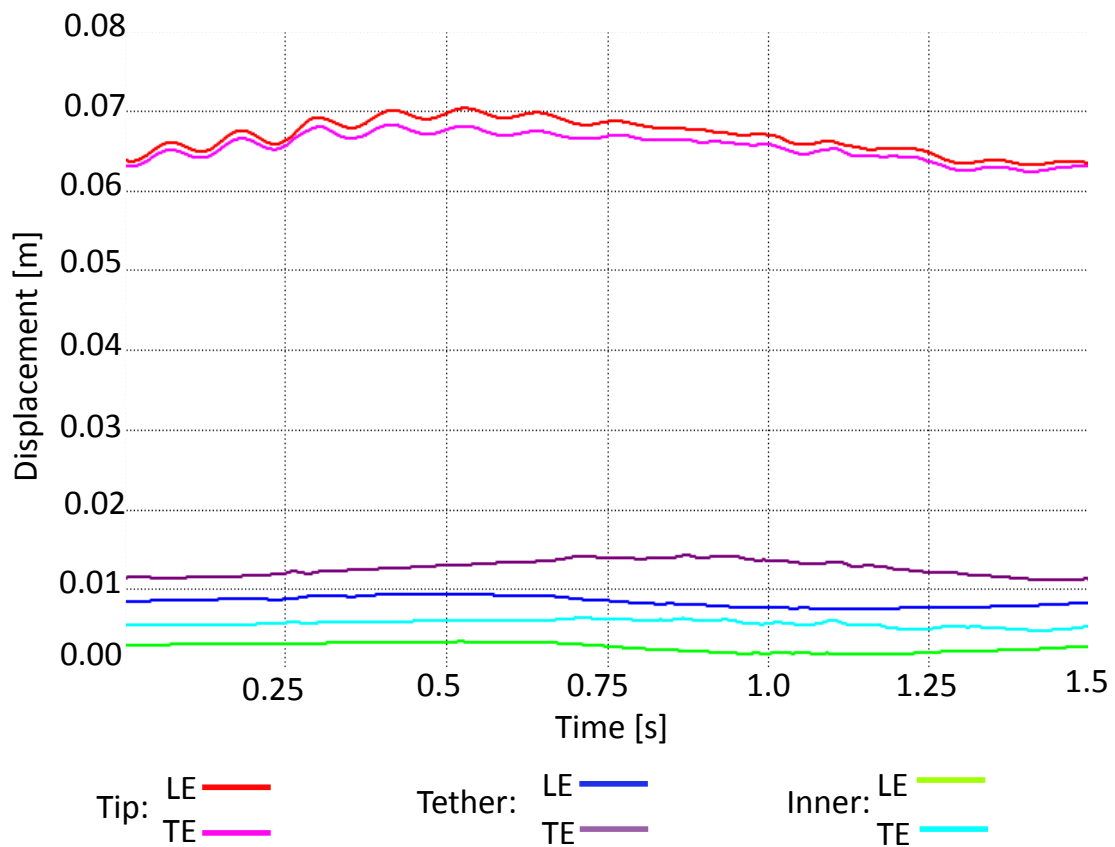


Figure 36: Displacement during gust interaction for case 3 actuation

4.3 Loads

The normalized force for the FSI simulation before the gust interaction is shown in figure 37. Here the force of the steady CFD simulation is shown as well. In comparison to the steady state CFD simulation the lift force is increased with 1.24% in the FSI simulation after it has reached a less oscillating state and before the gust hits the wing. This is due to the deformation of the wing. However, the displacements on the trailing and leading edge indicate that only the outer part of the wing, outside of the tether, attachment has an increase in AoA whereas the rest of the wing has a slight decrease in AoA. This might seem contradictory, a decrease of AoA generally means a smaller force acting on the wing. However, one must also take into account that there is a deformation of the wing, not only a pitching motion. Hence the comparison between a steady state lift force and the FSI lift force cannot be explained simply with the change of AoA. The deformation over the entire wing must be taken into account as well.

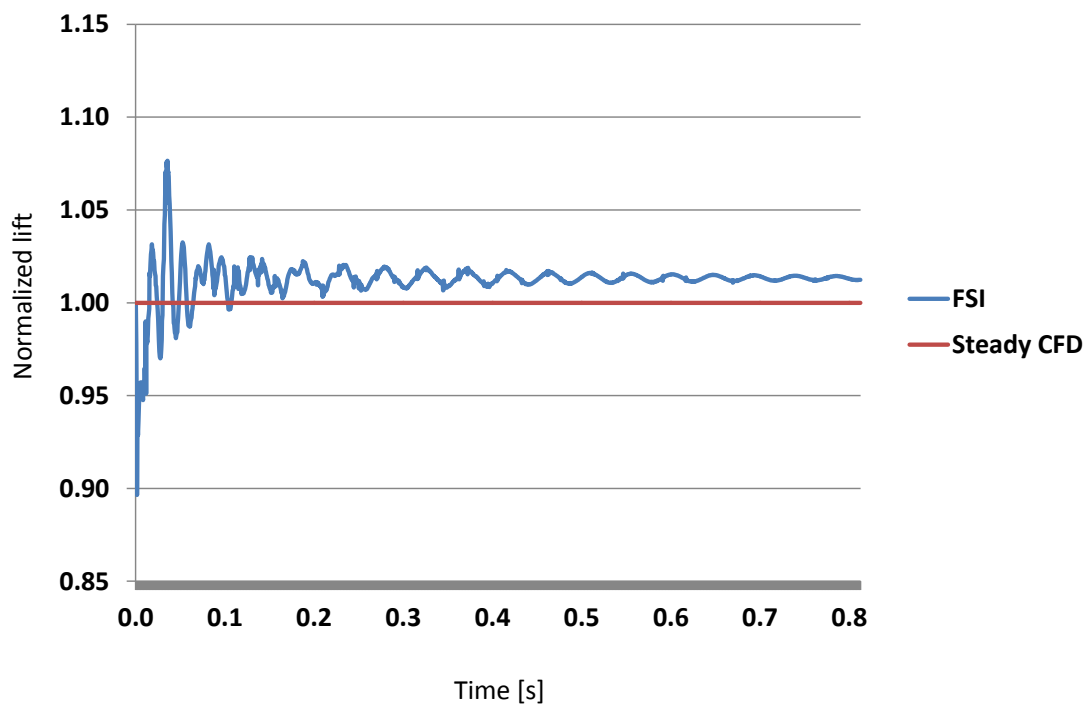


Figure 37: Normalized lift for FSI simulation before gust interaction

Figure 38 shows the normalized lift for the different cases starting from time 0 when the gust interaction starts. It can be seen that without any actuation the normalized lift varies with the change in freestream velocity. This indicates that the wing experiences the wind gust the way it was intended. At most the gust load increases the normalized lift with around 14%.

It is clear that in case 1 the actuation is not strong enough to alleviate the entire load induced by the gust wind. The gust hits the wing, increasing the lift force with approximately 5%, before the actuation starts. There is still a 10% increase in lift when the gust is at its strongest. However, in comparison to the gust wind without actuation there is still 4% load alleviation. At

the end of the actuation the normalized lift is negative. This is expected due to the delay of the actuation in comparison to the gust.

In case 2 there is a stronger load alleviation as expected. It quickly deviates from case 1 and clearly decreases the load approximately 40% more than in the case 1, from 10% increase to 6% increase in normalized lift. For this case the negative normalized lift is stronger at the end of the cycle which is expected due to the stronger actuation.

The same trend is followed in case 3; stronger load alleviation followed by a stronger decrease in normalized lift at the end of the cycle. The results show that the actuation of case 3 is much too strong for a gust wind of this magnitude.

At the second half of the gust simulation the normalized lift for case 3 starts to behave unexpectedly just like the result for the displacements. This is once again by separation that occurred locally on the wing. With this in mind it seems that the upper limit for the actuation strategy is controlled by the increased local camber of the wing rather than the magnitude of the gust.

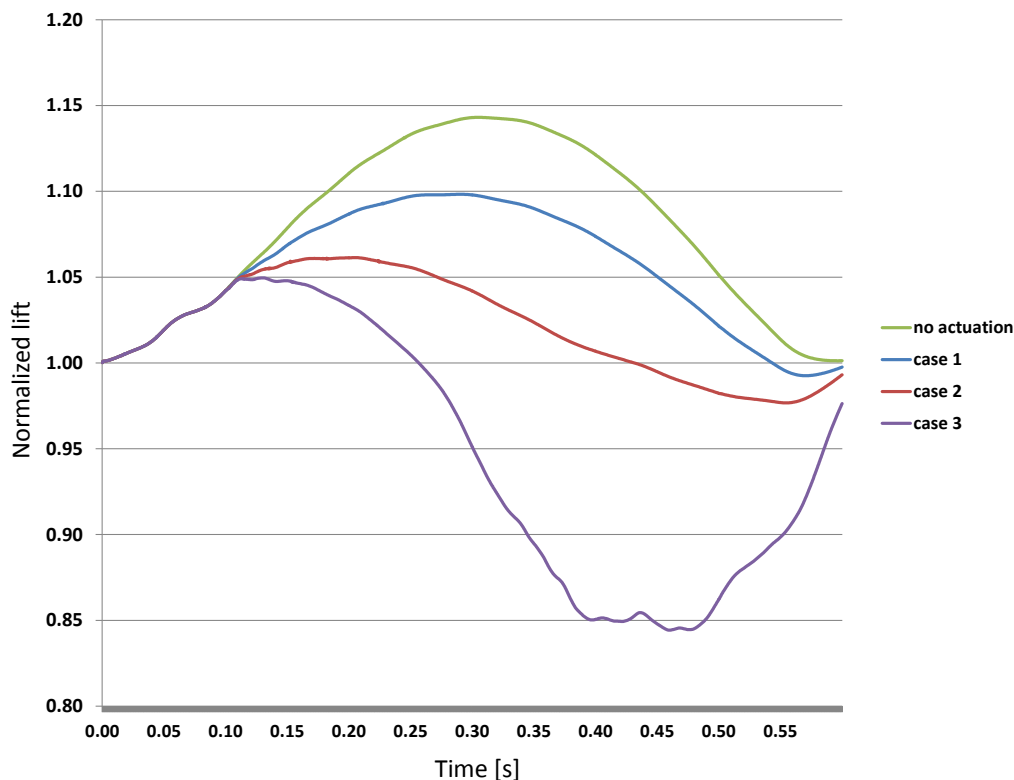


Figure 38: Normalized lift during gust interaction for different actuation strategies

There is no linear relationship between the load alleviation of the different cases and some kind of calibration is needed to improve the actuation for the gust wind. For this wing case 2 would give a good load alleviation for a gust wind with an amplitude of 5 m/s. Furthermore it is clear that the delay of the actuation is of great importance. A delay of 0.01 seconds instead of 0.1 seconds would yield better results, considering the load would not increase the initial 5% before the actuation starts. This can be changed in the setup of the simulation.

An interesting observation is that even though the difference in displacement of the different cases are relatively small, the change in force has a large influence. This indicates that a small change is needed in actuation for a significant load alleviation.

5 Conclusion and outlook

A high fidelity FSI simulation environment for analysing transient gust load alleviation with morphing AWE wings has successfully been set up. The simulation environment also offers the possibility of investigating dynamic instabilities.

An automatic mesh generation has been created using the software ICEM CFD. It generates a high quality hexahedral mesh for an arbitrary AWE wing with minimum user input.

Different ways of simulating gust winds have been investigated and implemented as part of the tool. The Forcing Momentum Source was chosen as the most appropriate and makes it possible for to specify the shape, amplitude and duration for the gust simulation.

A possible improvement of the wing would be the addition of wingtip devices. However, further investigation on whether the addition would increase the efficiency of the system is needed. Another strategy would be to change the shape of the wingtip, for example to a more elliptical shape. This could also lead to a reduced induced drag.

A recirculation region appears at the wing tip. This could be avoided by making the wingtip more aerodynamically efficient, for example by making the angle between the leading edge and the wingtip less steep and more rounded.

The FSI results show a slightly higher lift force acting on the wing before the gust hits it in comparison to the steady state simulation. This is most likely due to the deformations of the wing. No dynamic instabilities occurred on the wing at a freestream velocity of 100 m/s during the simulation time. The gust response of the wing without actuation shows a relation between the increased freestream velocity and the lift force on the wing as expected.

Furthermore, high-fidelity FSI simulation has been carried out on a morphing AWE wing. The FSI includes gust interaction and different actuation strategies for load alleviation. Three different cases were simulated with different actuation strength. The results show that the delay of the actuation is of great importance to the load alleviation. Furthermore, the actuation strength needs to be calibrated in order to achieve a certain load alleviation capability. This is possible to do within the simulation environment created in this thesis.

5.1 Outlook

An investigation of the influence of nonlinearity for the structural solver should be made to see if it has a significant influence on the solution

It would also be interesting to investigate the influence of the circular flight pattern for the AWE system more closely. This could for example be done as a steady state CFD simulation with a rotating reference frame. This would give an idea of the size of the approximation with a straight flight path.

Because there is no obvious relation between actuation and load alleviation a calibration of the morphing would be interesting. This can be done by decreasing the delay and tune the actuation of the wing in order to make it possible to alleviate gusts of a certain magnitude. This is all possible to do within the simulation environment created in this thesis.

Another interesting feature would be to control the actuation based on the freestream velocity instead of presetting the thermal boundary conditions for the structure. This could be done by using a probe that measures the velocity in the freestream at a point upstream of the wing. Any change in the velocity could be transferred to the structural solver and indicate a certain amount

of actuation for the wing. This application would also be possible for a real system which make for a more realistic actuation simulation. In reality the probe could be placed for example 2 meters ahead of the wing. At a wind speed of 100 m/s this would mean the probe would register the change in the freestream velocity 0.02 seconds before it hits the wing. This would also be the time the system have to start its actuation in order to actuate with the change in wind speed accordingly.

A feature that would increase the efficiency and robustness of the tool is a way to ramp the aerodynamic loads acting on the wing in the beginning of the simulation. If this can be made the large oscillations that occur at first could be minimized and solution would reach a more steady state earlier, reducing the time before the gust simulation can start. Smaller displacements are also easier for the fluid solver to handle when it comes to morphing the mesh.

Bibliography

- [1] R. M. Ajaj, C. S. Beaverstock, and M. I. Friswell, "Morphing aircraft: The need for a new design philosophy," *Aerospace Science and Technology*, vol. 49, pp. 156–166, 2011.
- [2] M. Asif and T. Muneer, "Energy supply, its demand and security issues for developed and emerging economies," *Renewable and Sustainable Energy Reviews*, vol. 11, pp. 1461–1476, 2007.
- [3] U. Ahrens, M. Diehl, and R. Schmehl, *Airborne Wind Energy*. Springer, 2014.
- [4] A. Cherubini, A. Papini, R. Vertechy, , and M. Fontana, "Airborne wind energy systems: A review of the technologies," *Renewable and Sustainable Energy Reviews*, vol. 51, pp. 1461–1476, 2015.
- [5] Makani Power, www.makanipower.com, 2017.
- [6] SwissKitePower , www.swisskitepower.ch, 2017.
- [7] KiteGen , www.kitegen.com, 2017.
- [8] M. L. Loyd, "Crosswind kite power," *Journal of Energy*, vol. 4, no. 3, pp. 106–111, 1980.
- [9] A. R. Rodriguez, "Morphing aircraft technology survey," *AIAA Paper 2007-1258*, January 2007.
- [10] T. A. Weisshaar, "Morphing aircraft systems: Historical perspectives and future challenges," *Journal of Aircraft*, vol. 50, no. 2, 2013.
- [11] R. W. Wlezien, G. C. Horner, A. R. McGowan, S. L. Padula, M. A. Scott, R. J. Silcox, and J. O. Simpson, "The aircraft morphing program," *AIAA Paper 1998-1927*, 1998.
- [12] O. H. Ammann, T. von Kármán, and G. B. Woodruff), "The failure of the tacoma narrows bridge," 1943. <http://resolver.caltech.edu/CaltechAUTHORS:20140512-105559175>, 2017.
- [13] X. Chen, G.-C. Zha, and M.-T. Yang, "numerical simulation of 3-d wing flutter with fully coupled fluid-structure interaction," *Computers and Fluids*, vol. 36, pp. 856–867, 2007.
- [14] R. Torii, M. Oshima, T. Kobayashi, K. Takagi, and T. E. Tezduyar, "Fluid-structure interaction modeling of blood flow and cerebral aneurysm: Significance of artery and aneurysm shapes," *Computat. Methods Appl. Mech. Engrg*, vol. 198, pp. 3613–3621, 2009.
- [15] U. Fasel, D. Keidel, G. Molinari, and P. Ermanni, "Aerostructural optimization of a morphing wing for airborne wind energy applications," *In progress*.
- [16] A. M. Wickenheiser and E. Garcia, "Extended nonlinear liftin-line method for aerodynamic modeling of reconfigurable aircraft," *NASA Technical Memorandum 110148*, September 1995.
- [17] XFOIL, http://web.mit.edu/aeroutil_v1.0/xfoil_doc.txt, 2017.
- [18] D. E. Raveh, "Cfd-based gust response analysis of free elastic aircraft," *AIAA Paper 2009-2539*, June 2009.

- [19] P. Lancelot, J. Sodja, N. Werter, and R. D. Breuker, "Design and testinf of a low subsonic wind tunnel gust generator," *Proc. of International Forum on Aeroelasticity and Structural Dynamics*, June 2015.
- [20] IEC, "Wind tirbines - part1: Design requirements," *IEC 61400-1: Third edition 2005-08*.
- [21] Anon., "Gust and turbulence loads," *Code of Federal Regulations, Aeronautics and Space, Section 25.341*, pp. 401–402, 1996.
- [22] J. D. Andersson, *Fundamentals of Aerodynamics*. Fifth edition, McGraw-Hill, 2011.
- [23] D. McLean, *Understanding Aerodynamics*. WILEY, 2013.
- [24] G. K. Batchelor, *An Introduction to Fluid Dynamics*. Cambridge University Press, 1967.
- [25] ANSYS Inc., *Fluent Theory Guide*, v. 17.0.
- [26] L. F. Richardson, *Weather Prediction by Numerical Process*. Cambridge University Press, 1922.
- [27] S. B. Pope, *Turbulent Flows*. Cambridge University Press, 2000.
- [28] J. Boussinesq, "Essai sur la théorie des eaux courantes," *Mémoires présentés par divers savants à l'Académie des Sciences*, 1887.
- [29] J. Kim, P. Moin, and R. Moser, "Turbulence statistics in fully developed channel flows at low reynolds number," *Journal of Fluid Mechanics*, vol. 177, pp. 133–166, 1986.
- [30] F. R. Menter, M. Kuntz, and R. Langtry, "Ten years of industrial experience with the sst turbulence model," *Proc. Turbulence, Heat and Mass Transfer*, eds.: Hanjalic, K., Nagano, Y and Tummers, M, 2003.
- [31] F. R. Menter, "Two-equation eddy-viscosity turbulence models for engineering applications," *AIAA Journal*, vol. 32, no. 8, pp. 1598–1605, 1994.
- [32] F. R. Menter, "Zonal two equation $k-\omega$ turbulence models for aerodynamic flows," *AIAA Journal*, vol. 32, no. 8, pp. 1598–1605, 1994.
- [33] F. R. Menter, "Improved two-equation $k-\omega$ turbulence moddels for aerodynamic flows," *Nasa Technical Memorandum 103975*, 1992.
- [34] P. R. Spalart and S. R. Allmaras, "A one-equation turbulence model for aerodynamic flows," *AIAA paper 92-G439*, 1992.
- [35] J. Tu, G. Yeoh, and C. Liu, *Computational Fluid Dynamics A Practical Approach*. Second edition, ELSEVIER, 2013.
- [36] ANSYS Inc., *Mechanical APDL Theory Reference*, v. 17.0.
- [37] M. Heil, A. L. Hazel, and jonathan Boyle, "Solvers for large-displacement fluid-structure interaction problems: segregated versus monotholic approaches," *Journal of Computational Mechanics*, vol. 43, pp. 91–101, 2008.

- [38] R. Sanches, R. Palacios, T. D. Economon, H. L. Kline, J. J. Alonso, and F. Palacios, "Towards a fluid-structure interaction solver for problems with large deformations within the open-source su2 suite," *Journal of Fluid Mechanics*, vol. 177, pp. 133–166, 1986.
- [39] J. Degroote, K.-J. Bathe, and J. Vierendeels, "Performance of a new partitioned procedure versus a monolithic procedure in fluid-structure interaction," *Computers and Structures*, vol. 87, pp. 793–801, 2009.
- [40] ANSYS Inc., System Coupling User's Guide, v. 17.0.
- [41] ANSYS Inc., www.ansys.com, 2017.
- [42] P. R. Spalart and C. L. Rumsey, "Effective inflow conditions for turbulence models in aerodynamic calculations," *AIAA Journal*, vol. 45, no. 10, 2007.
- [43] G. Molinari, M. Q. A. Arrieta, M. Morari, and P. Ermanni, "Design, realization and structural testing of a compliant adaptable wing," *Smart Materias and Structures*, vol. 24, 2015.
- [44] V. Vandecaeter, "Cfd simulation of atmospheric wind gusts," *Master Thesis*, 2011.
- [45] D. P. Lockard and P. J. Morris, "Radiated noise from airfoils in realistic mean flows," *AIAA Journal*, vol. 36, no. 6, pp. 907–914, 1998.
- [46] V. V. Golubev, T. M. Hollenshade, L. Nguyen, and M. R. Visbal, "Parametric viscous analysis of gust interaction with sd7003 airfoil," *AIAA Paper 2010-928*, 2009.
- [47] V. V. Golubev, T. M. Hollenshade, L. Nguyen, N. V. Golubev, and M. R. Visbal, "High-accuracy viscous simulations of gust interaction with stationary and pitching wing sections," *AIAA Paper 2009-0011*, 2009.
- [48] V. V. Golubev, B. D. Dreyer, T. M. Hollenshade, and M. R. Visbal, "High-accuracy viscous simulations of gust-airfoil nonlinear aeroelastic interation," *AIAA Paper 2009-4200*, 2009.
- [49] E. H. Dowell, *A Modern Course in Aeroelasticity*. fifth edition, Springer, 1989.
- [50] Z. T. Applin, "Pressure distributions from subsonic tests of a naca 0012 semispan wing model," *AIAA Paper 98-0597*, 1995.
- [51] D. B. Owens, "Weissinger's model of the nonlonear lifting-line method for aircraft design," *AIAA Paper 98-0597*, 1998.

A Diffusion based dynamic mesh theory

Following is the theory of diffusion based smoothing. The method is governed by the diffusion equation.

$$\nabla \cdot (\gamma \nabla \vec{u}) = 0 \quad (\text{A.1})$$

here \vec{u} is the displacement vector and γ the diffusion coefficient. In order to keep the mesh attached to a moving boundary, the mesh motion on at that boundary is set to tangent as a boundary condition. This leaves the mesh motion to vanish. Equation A.1 then describes how the mesh should diffuse into the mesh.

Depending on how the diffusion coefficient is defined the motion of the mesh will spread differently though out the mesh. Two different strategies can be chosen for the diffusion based smoothing method: the boundary-distance method and the volume based method. The boundary-distance method increases the motion of the mesh based on the distance to the moving boundary. In this method γ is defined as:

$$\gamma = \frac{1}{d^a} \quad (\text{A.2})$$

The other alternative is the volume based smoothing method. Here cells with larger volume tends to absorb most of the motion, leaving smaller cells less influenced. Here the diffusion coefficient is defined as:

$$\gamma = \frac{1}{V^a} \quad (\text{A.3})$$

a in the two methods can be set to a certain value indicating how strong the effect of the volume and the boundary distance have on the morphing. A value of 0 means equal morphing in the mesh.

B Implementation of gust UDFs

Following is the implementation of respective gust simulation. They are implemented as user defined functions in Fluent, where C is used as coding language. It is advised to copy the source term of interest into a C compiler in order to more easily understand the code. Furthermore, `/*` comment `*/` implies a comment in C.

The artificial gust has a moving inlet boundary condition on the upper and lower boundary. The whole boundary is specified as an inlet boundary condition but outside of the gust region the inlet- and outlet velocities are set to zero and the velocity in x-direction is set to the freestream velocity.

Concerning the vortex momentum source method, as mentioned in the report it is a much more complicated implementation in comparison to the other two. The reader is strongly advised to look into the article where the source term is explained to fully understand and implement the source term [47, 47, 48]. The values implemented are also taken from these articles.

The Forcing Momentum Source term can be implemented in any direction.

Moving boundary up

```
#include "udf.h"

DEFINE_PROFILE(moving_gust_y_up, thread, i)
{

real A0 = 7.5; /* height to center point */
real Wg = 20.0; /* amplitude gust */
real Lg = 5.0; /* length gust */
real Vg = 10.0; /* speed gust */
real pi = 3.14159265359;
face_t f; /* face thread variable */
real x[ND_ND];
real t=CURRENT_TIME;
real t1=0.0; /* start time gust */
real x_0;
real start_domain = 15;

begin_f_loop(f, thread)

{
    F_CENTROID(x,f,thread);
    x_0=x[0];
    real time=(t-t1);

    if(0<=time)
    {
        if(((Vg*time)-start_domain)<=x_0 && x_0<=((Vg*time+Lg)-start_domain))
        {
            F_PROFILE(f,thread,i) = (Wg*pi*A0*sin(2*pi*(time-(x_0/Vg))*(Vg/Lg)))/Lg;
        }
        else
        {
            F_PROFILE(f,thread,i)=0.0;
        }
    }
    else
    {
        F_PROFILE(f,thread,i)=0.0;
    }
}
end_f_loop(f, thread)
}
```


Moving boundary down

```
#include "udf.h"

DEFINE_PROFILE(moving_gust_y_down, thread, i)
{

real A0 = 7.5; /* height to center point */
real Wg = 20.0; /* amplitude gust */
real Lg = 5.0; /* length gust */
real Vg = 10.0; /* speed gust */
real pi = 3.14159265359;
face_t f; /* face thread variable */
real x[ND_ND];
real t=CURRENT_TIME;
real t1=0.0; /* start time gust */
real x_0;
real start_domain = 15;

begin_f_loop(f, thread)

{
    F_CENTROID(x,f,thread);
    x_0=x[0];
    real time=(t-t1);

    if(0<=time)
    {
        if(((Vg*time)-start_domain)<=x_0 && x_0<=((Vg*time+Lg)-start_domain))
        {
            F_PROFILE(f,thread,i) = -(Wg*pi*A0*sin(2*pi*(time-(x_0/Vg))*(Vg/Lg)))/Lg;
        }
        else
        {
            F_PROFILE(f,thread,i)=0.0;
        }
    }
    else
    {
        F_PROFILE(f,thread,i)=0.0;
    }
}
end_f_loop(f, thread)
}
```

Vortex momentum source x-direction

```
#include "udf.h"

DEFINE_SOURCE(source_vortex_x, c,t,dS,eqn)
{

real x[ND_ND];
C_CENTROID(x,c,t)
real x_0 = x[0];
real y_0 = x[1];

real freestream_u = 5; /* THIS COULD MAYBE BE USED AS C_U(c,t) instead */

real pi = 3.14159265359;
real alfa = 4; /*airfoil c*/
real beta = 4; /*freq. param*/
real omega_g = 4; /*gust frequensy*/
real eps_g = 0.1; /*gust intensity*/

real x_s = -1.5; /*locations for source term*/
real y_s = 2; /*locations for source term*/
real b = 5; /*locations for source term*/
real g;
real time = CURRENT_TIME;

/*loop?*/

real lambda = 0.5* (tanh(3 * (y_0 + y_s) - tanh(3 * (y_0 - y_s))));
real K = (eps_g*((alfa * freestream_u * freestream_u) * ((alfa * alfa) - (b * b)))) / (sqrt((alfa * alfa) +
(beta * beta)) * b * b * sin((omega_g * pi) / (freestream_u * b))); /*constant*/

if(abs(x_0 - x_s) <= (pi / b))
    {
        g = 0.5*(1+cos(b*(x_0-x_s)));
    }
    else
        {
            g=0.0;
        }

real source = beta * K * g * lambda * cos((omega_g * time) - (beta * y_0) - (alfa * x_s)); /* whatever
yuor source is */

dS[eqn]=0.0; /* derivative source term? */
return source;

}
```

Vortex momentum source y-direction

```
#include "udf.h"

DEFINE_SOURCE(source_vortex_y, c,t,dS,eqn)
{

real x[ND_ND];
C_CENTROID(x,c,t)
real x_0 = x[0];
real y_0 = x[1];

real freestream_u = 5; /* freestream velocity */

real pi = 3.14159265359;
real alfa = 0.6; /* airfoil c */
real beta = 4; /* freq. param */
real omega_g = 4; /* gust frequensy */
real eps_g = 0.1; /* gust intensity */

real x_s = -1.5; /* locations for source term */
real y_s = 2; /* locations for source term */
real b = 5; /* locations for source term */
real g_der;
real time = CURRENT_TIME;

/*loop?*/

real lambda = 0.5* (tanh(3 * (y_0 + y_s) - tanh(3 * (y_0 - y_s))));
real K = eps_g*((alfa * freestream_u * freestream_u) * ((alfa * alfa) - (b * b))) / (sqrt((alfa * alfa) +
(beta * beta)) * b * b * sin((omega_g * pi) / (freestream_u * b))); /* constant */

if(abs(x_0 - x_s) <= (pi / b))
{
g_der = (-b*sin(b*(x_0-x_s))/2);
}
else
{
g_der=0.0;
}

real source = K * g_der * lambda * cos((omega_g * time) - (beta * y_0) - (alfa * x_s)); /* whatever
your source is */
dS[eqn]=0.0; /* source term derivative */

return source;

}
```

Forcing momentum source term

```
#include "udf.h"

DEFINE_SOURCE(source_force_vel, c,t,dS,eqn)
{

real x[ND_ND];
C_CENTROID(x,c,t)
real pi = 3.14159265359;

real real_time = CURRENT_TIME;
real time_step = CURRENT_TIMESTEP;
real start_time_gust = 0.5; /* time start gust */
real length_gust = 0.5; /* time length gust */
real end_time_gust = start_time_gust + length_gust;
real gust_time = (real_time - start_time_gust);
real gust;

real u_freeS = 100; /* freestream velocity */
real gust_amp = 5; /* amplitude gust */
real speed = (C_R(c,t) * 3 / time_step);
/* constant in order to get the right units, increase the value to increase speed of convergence */

real z_up = 13; /* how far in z-direction the source term is acting (must keep a few elements
unaffected by the source term)*/

    if(0 <= gust_time && gust_time <= end_time_gust && z_0 <= z_up)
    {
        gust = ((u_freeS + gust_amp * sin(1 * pi * (gust_time/length_gust))) - C_U(c,t)) * speed;
        /*
        sinusoidal: gust_amp * sin(1 * pi * (gust_time/length_gust) );
        linear: gust_amp * gust_time/ length_gust;
        1-cosine: gust_amp * 0.5*(1-cos((gust_time/gust_length)*2*pi));
        EOG: gust_amp*-0.5 *sin(3*pi*gust_time/gust_length)* (1cos(2*pi*gust_time/gust_length));
        */

        dS[eqn] = -speed; /* derivative for source term (dS/du) */
    }
    else
    {
        gust = dS[eqn] = 0;
    }

real source = gust;
return source;
}
```